

High Temperature Superconductivity in Iron Pnictides and Chalcogenides

Qimiao Si¹, Rong Yu^{2,3} & Elihu Abrahams⁴

¹*Department of Physics and Astronomy, Rice University, Houston, TX 77005, USA*

²*Department of Physics and Beijing Key Laboratory of Opto-electronic Functional Materials and Micro-nano Devices, Renmin University, Beijing 100872, China*

³*Department of Physics and Astronomy, Collaborative Innovation Center of Advanced Microstructures, Shanghai Jiaotong University, Shanghai 200240, China*

⁴*Department of Physics and Astronomy, University of California Los Angeles, Los Angeles, CA 90095, USA*

Superconductivity develops in metals upon the formation of a coherent macroscopic quantum state of electron pairs. Iron pnictides and chalcogenides are materials that have high superconducting transition temperatures. In this Review, we describe the advances in the field that have led to higher superconducting transition temperatures in iron-based superconductors and the wide range of materials that form them. We summarize both the essential aspects of the normal state and the mechanism for superconductivity. We emphasize the degree of electron-electron correlations and their manifestation in properties of the normal state. We examine the nature of magnetism, analyse its role in driving the electronic nematicity, and discuss quantum criticality at the border of magnetism in the phase diagram. Finally, we review the amplitude and structure of the superconducting pairing, and survey the potential settings for optimizing superconductivity.

In early 2008, the discovery of superconductivity with a transition temperature (T_c) of 26 K in an iron pnictide compound took the condensed matter and materials physics community by surprise¹. It raised the prospect for high-temperature superconductivity beyond the copper-based materials, the only materials known up to then having a T_c higher than 40 K.² While the transition temperature in the iron pnictides was quickly raised to 56 K in a matter of a few months³, that record did not change for several years. However, recent

developments in the iron chalcogenides⁴⁻⁸ have given renewed hope for even higher transition temperatures. Meanwhile, considerable progress has been made on the understanding of the microscopic physics of these iron-based superconductors (FeSCs).

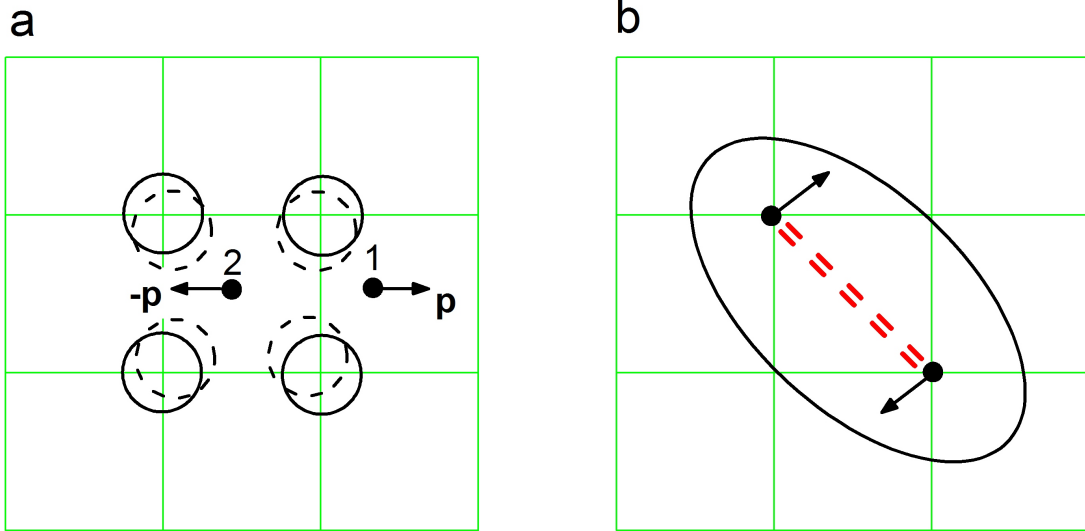


FIG. 1. Illustration of superconducting pairing. a. Conventional superconductivity. Ionic vibrations mediate attraction between two electrons of opposite momenta. Electron 1 leaves a distortion of the ions (circles), which provides attraction for electron 2 with opposite momentum. Because of a time delay, the Coulomb repulsion between the electrons is avoided. b. Unconventional superconductivity. In order to lower their energy, a pair of electrons avoids the Coulomb repulsion by means of spatial anisotropy in their relative motion. In this process, an attractive coupling (double-dashed line) is generated.

Superconductivity was discovered by H. Kamerlingh Onnes over a century ago⁹. In a remarkable 1957 paper, the phenomenon was explained by J. Bardeen, L. Cooper and J. R. Schrieffer (“BCS”)¹⁰. Superconductivity develops when electron pairs are condensed, that is, they move in unison and conduct electricity without experiencing any resistive loss of energy. In the BCS theory, electrons form pairs through an attractive interaction mediated by phonons, the quantized ionic vibrations, At the same time, Coulomb repulsion is avoided because a pair is formed between electrons with a time delay, as shown in Fig. 1a.

In the FeSCs, superconductivity pairing does not arise from the conventional electron-phonon coupling¹¹, and is instead a consequence of an unconventional pairing mechanism

generated by the electron–electron Coulomb interaction. Qualitatively, electrons form pairs by an attractive force produced in the process of avoiding their Coulomb repulsion, as illustrated in Fig. 1b.

Two important characteristics of the FeSCs provide clues to the mechanism for their unconventional superconductivity: In the FeSC phase diagram, superconductivity emerges out of a “bad-metal” normal state; and the superconducting phase occurs near an AF order. This has led to extensive experimental and theoretical studies on the effect of electron correlations and the nature of magnetism in the iron pnictides and chalcogenides. In the process, several significant properties have been discovered. One is electronic nematicity and its relationship to magnetism. Another concerns quantum criticality which arises at the border of the AF order. All these effects are also intimately connected to the amplitude and structure of the superconducting pairing.

The purpose of the present article is several fold. We first summarize the materials basis and electronic structures for the FeSCs. We then present a status report on key aspects of the microscopic physics. At the present time, a variety of theoretical approaches are being taken to understand these systems. Rather than describing any theoretical framework, we have organized this part of the article by considering the hierarchy of the significant energy scales in these materials: Coulomb repulsion with an order of magnitude of 1 eV, followed by the energy scale for the antiferromagnetism, of order 0.1 eV and reaching down to the superconductivity, whose pairing energy scale is on the order of 0.01 eV. Our conclusion includes a discussion of the prospects for further discoveries and understandings as well as the implications such studies have for the overall field of unconventional superconductivity.

I. MATERIALS BASIS AND ELECTRONIC STRUCTURES

FeSCs have an extensive materials basis. Fig. 2a illustrates the structure of several iron pnictides and chalcogenides. A common feature in all these materials is the existence of either Fe-pnictogen or Fe-chalcogen trilayers. In each FeAs/FeSe trilayer, the Fe ions form a square lattice, and the As/Se atoms are located above or below the center of a square plaquette of the Fe ions. LaFeAsO belongs to the 1111 iron-pnictide family, comprising FeAs trilayers that are separated by LaO layers. The maximum $T_c = 56$ K in the 1111 family is achieved in the SmFeAsO system with F-doping³. BaFe₂As₂ belongs to the 122 iron-pnictide

family²³. Here, each unit cell contains two FeAs trilayers, which are separated by a layer of Ba ions. Superconductivity arises by chemical substitution into the undoped compound, as illustrated in Fig. 2b for the case of Ni_x substitution into BaFe_2As_2 . The maximum T_c that has been reached in such 122 iron pnictides is 38 K, occurring in $\text{Ba}_{0.6}\text{K}_{0.4}\text{Fe}_2\text{As}_2$.

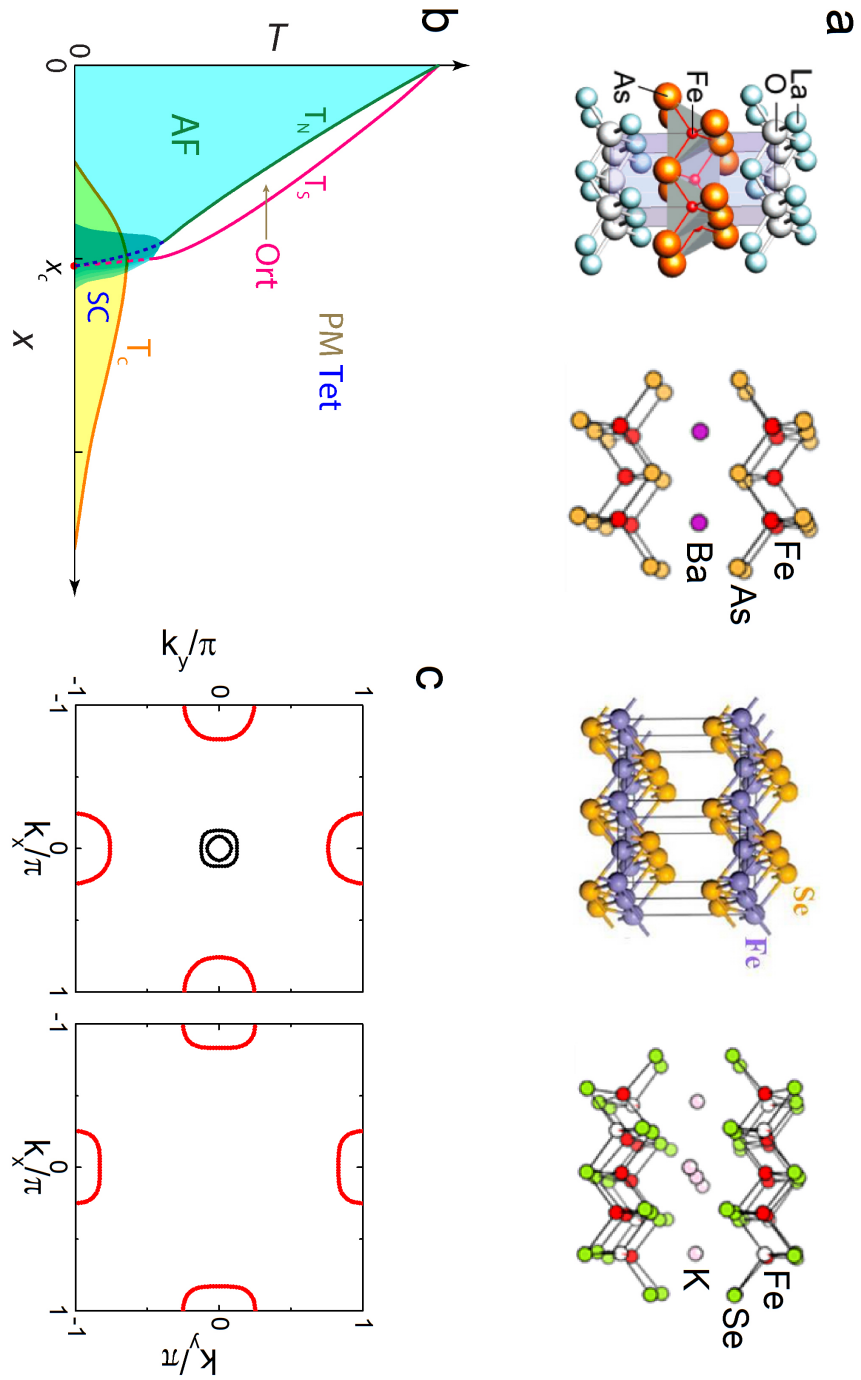


FIG. 2. Materials characteristics of the iron-based superconductors. a: Crystal structure of LaFeAsO (1111), BaFe₂As₂ (122), FeSe (11) and K_xFe_{2-y}Se₂. Adapted from Refs. 1, 151, and 24. b: Schematic phase diagram of BaFe_{2-x}Ni_xAs₂ in the temperature (T) and chemical-substitution (x) plane. Adapted from Ref. 27. c: Schematic Fermi surfaces of the iron pnictides (left panel) and those of several iron-chalcogenides (right panel, see main text). Adapted from Ref. 21.

Also shown in Fig 2a are two representative families of iron chalcogenides. FeSe has the simplest structure in this category²⁴, with each unit cell being an FeSe trilayer. Each FeSe trilayer corresponds to an Se-for-As replacement of an FeAs trilayer. The potassium iron selenides^{25,26} K_xFe_{2-y}Se₂, can be viewed as derived from the FeSe system by inserting K ions between two FeSe trilayers. In these bulk iron selenides, the maximum T_c that has been reached is similar to that of the 122 iron pnictides. More recently, “single-layer” FeSe on SrTiO₃ substrate (“STO”) has been fabricated^{4,6}. In this material, there has been substantial evidence for superconductivity up to 65 K, as indicated by the opening of a gap in the electron spectrum⁵ and the onset of Meissner effect⁷, as well as a report of T_c of 109 K, as evidenced by electrical transport measurements⁸.

Despite the similarities in their crystal structures, an important feature for the FeSCs is a large variation of their electronic structures. This is highlighted by the Fermi surfaces. Fig. 2c illustrates the typical Fermi surfaces of the iron pnictides, comprising hole Fermi pockets in the middle of the Brillouin zone and electron Fermi pockets at the boundaries of the Brillouin zone²⁸. By contrast, in several iron chalcogenides, there are only electron Fermi pockets, as represented in the right-hand panel of Fig. 2c. This describes single-layer FeSe on STO substrate. It also applies to K_xFe_{2-y}Se₂, which however contains an additional electron pocket near the Γ point in the Brillouin zone (see later, Fig. 7b), and there is not any hole Fermi pocket. As yet another example, in a class of extremely hole doped FeSCs such as KFe₂As₂, the zone boundary electron-like Fermi surfaces are absent and have turned into tiny hole Fermi pockets after a Lifshitz transition²⁹. We note that Fig. 2c illustrates the Fermi surfaces in purely two-dimensional (2D) Brillouin zone of the one-Fe unit cell. In reality, they are only quasi-2D and “warp” (*i.e.* disperse) along the third direction of the wavevector space, to varying degrees in different iron-based materials.

II. ELECTRON CORRELATIONS AND BAD-METAL BEHAVIOUR

An important clue to the microscopic physics of the FeSCs comes from the early observation that the metallic phases of the iron pnictides and chalcogenides are all characterized by bad-metal properties, as we explain below. Experimental and theoretical studies of such bad-metal behavior have provided considerable insights into the degree of electron correlations in both these classes of materials.

A. Iron pnictides and chalcogenides as bad metals

Consider a representative iron arsenide, such as BaFe_2As_2 . It is metallic and develops AF order at a Néel temperature (T_N) which is about 140 K.¹⁵ As with the other iron-based compounds, above T_N it is a paramagnetic metal with a rather large electrical resistivity. Several of these compounds are sufficiently clean to allow the observation of quantum oscillations at low temperature. However, even these have a very large magnitude of electrical resistivity at room temperature. This signifies a bad metal by the Mott-Ioffe-Regel criterion³⁰, namely the mean free path ℓ is very short, on the order of inter-particle spacing: its product with the Fermi wavevector, $k_F\ell$ is of order unity. To estimate $k_F\ell$, one recognizes that there are $p = 4$ or 5 bands crossing the Fermi level (Fig. 2c). Based on the single-crystal in-plane resistivity at room temperature of about $400 \mu\text{Ohm-cm}$, the estimated $k_F\ell \approx 5/p \approx 1$ for each Fermi pocket. This should be contrasted to a good metal, such as Cr, for which the resistivity in the paramagnetic state just above the room temperature is about 40 times smaller³¹. Because electron-phonon scattering has a much smaller contribution to the resistivity, such a small value of $k_F\ell$ in the iron pnictides signifies strong electron-electron interactions^{12,32}.

A related signature of the strong electron correlations is a considerable reduction in the weight of the Drude peak of the optical conductivity. As illustrated in Fig. 3a, Qazilbash *et al*¹³ observed that the spectral weight in the Drude peak is about 30% of the value expected from non-interacting electrons. This reduction is quite sizable, on the same order as that seen in other bad metals such as the normal state of the doped cuprate superconductors and V_2O_3 , where correlation effects are of primary importance. A corollary is that about 70% of the spectral weight resides in an incoherent part, associated with electronic states away from the Fermi energy. Similar behavior has also been seen in various other iron pnictides³³.

The reduction of the Drude weight is accompanied by the mass renormalization observed in the angle-resolved photoemission spectroscopy (ARPES). In the iron arsenides,

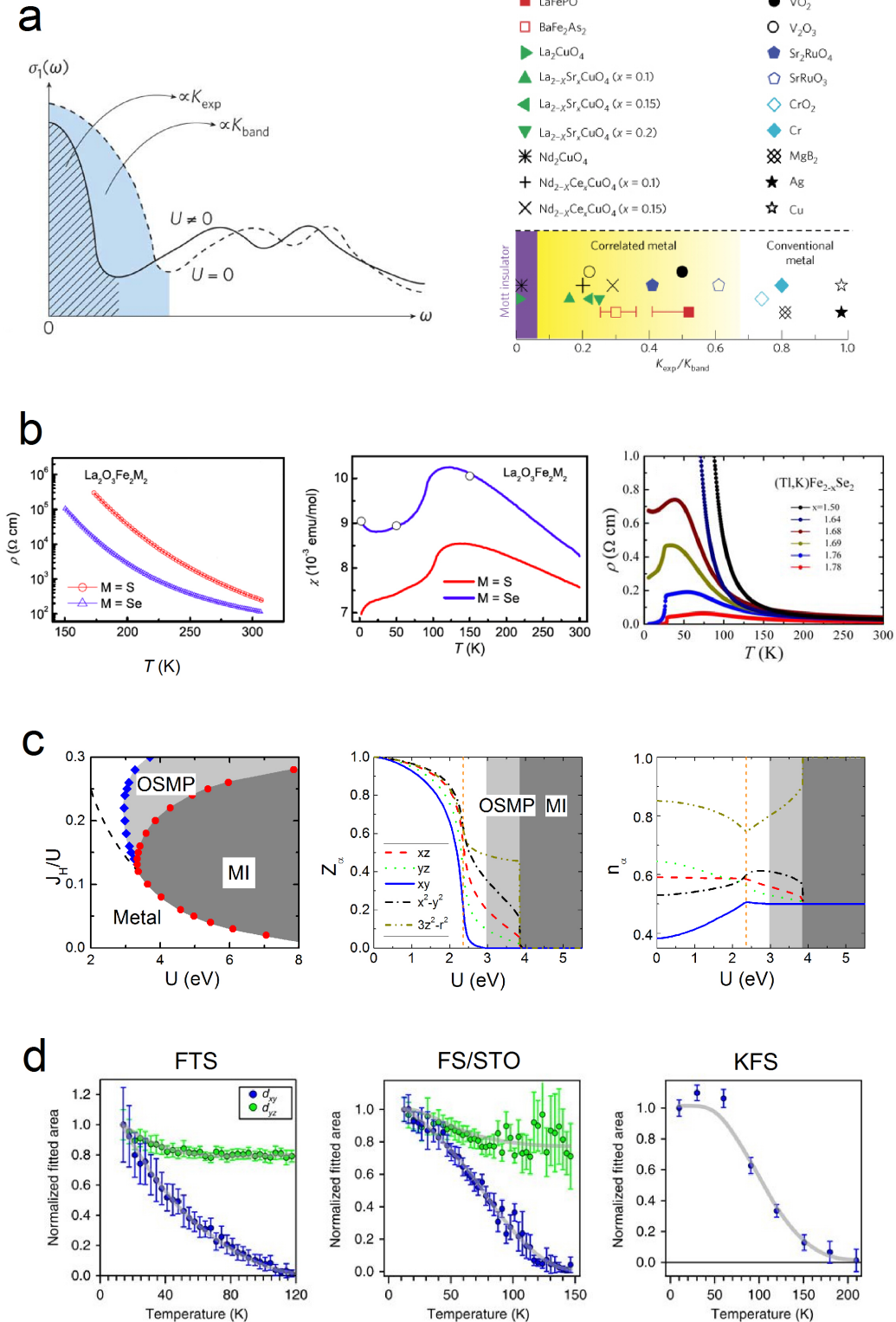


FIG. 3. Bad-metal behaviour and electron correlations. a: Left panel: Gauging electron correlations by the ratio of K_{exp} , the measured Drude weight of the optical conductivity $\sigma_1(\omega)$ vs. frequency ω , to K_{band} , its non-interacting counterpart. Adapted from Ref. 37. Right panel: K_{exp}/K_{band} for various systems, including the iron arsenides. From Ref. 13. b: Insulating iron chalcogenides. Left and middle panels: resistivity (ρ) and magnetic susceptibility (χ) vs. temperature T for the oxychalcogenides. From Ref. 38. Right panel: ρ vs. T for the alkaline iron selenides. From Ref. 39. c: Left panel: Ground-state phase diagram for the alkaline iron selenides at $N = 6$ (see the main text). The dark and light grey regions correspond to the Mott insulator (MI) and OSMP, respectively. The black dashed line describes a crossover into a strongly-correlated metal regime. Right panel: In the OSMP, the quasiparticle weight Z vanishes for the $3d\ xy$ orbital but is nonzero for the others; several orbitals are close to half-filling. From Ref. 40. d: Quasiparticle weight near the Fermi level determined from ARPES data for bands with distinct xy and yz characters, providing evidence for the OSMP in $\text{FeTe}_{0.56}\text{Se}_{0.44}$ (FTS, left panel), monolayer FeSe film on SrTiO_3 (FS/STO, middle panel), and $\text{K}_{0.76}\text{Fe}_{1.72}\text{Se}_2$ (KFS, right panel). From Ref. 36.

m^*/m in the paramagnetic phase is about 3–4.^{28,144} In the iron chalcogenides, in which the room-temperature resistivity also reaches the Mott-Ioffe-Regel limit, the effective mass enhancement can be as large as 20 for some of the involved bands^{34–36}.

These bad-metal properties suggest that the electron-electron correlations are sufficiently strong to place the metallic iron pnictides and chalcogenides in proximity of a Mott localization. Can we tune up the strength of the electron correlations and thereby push these and related materials into the Mott insulating state?

B. Mott insulators in the iron chalcogenides

A characteristic measure of the strength of the electron correlations is the ratio of the local electron-electron interaction to the electron bandwidth, or the kinetic energy. Therefore, reducing the kinetic energy would effectively enhance the correlation effects. This led to the consideration of the iron oxychalcogenides $\text{La}_2\text{O}_2\text{Fe}_2\text{O}(\text{Se,S})_2$. Like the FeAs trilayer of the iron pnictides, each $\text{Fe}_2\text{O}(\text{Se,S})_2$ layer contains a square lattice of Fe-ions, which also have a nominal valence of +2. However, the Fe-Fe distance has been increased, thereby leading

to a reduced kinetic energy. Calculations of their electronic structure demonstrated that their Fe 3*d*-electron bandwidth is about 75% of that in the usual cases such as LaFeAsO and BaFe₂As₂; the consequently enhanced electron correlation effects raised the possibility for a Mott insulating state in these materials³⁸. Experimentally, their insulating behavior is well-established by the temperature dependence of electrical resistivity, which shows an activated behavior with moderate charge gaps (0.19 eV and 0.24 eV, respectively for the Se and S cases) as shown in Fig. 3b, left panel. AF orderings occur around T_N of about 93 K and 105 K for the Se and S cases, respectively, as indicated by the temperature dependence of the magnetic susceptibility (Fig. 3b, middle panel) and neutron-scattering studies⁴¹. The insulating behavior persists above T_N , a characteristic signature of a Mott insulator⁴². Finally, the incoherent electronic excitations of such a correlated insulating state have recently been observed by X-ray spectroscopy⁴³.

Insulating behavior has also been observed in several other iron chalcogenides. One such case is the alkaline iron selenides³⁹, as shown in Fig. 3b, right panel. This corresponds to a “245” composition A_{0.8}Fe_{1.6}Se₂ (A=K,Tl/K,Rb), in which one out of five Fe-atoms is absent in each FeSe trilayer⁴⁴. It has been suggested that the ordered vacancies reduce the kinetic energy and, in a way similar to the oxychalcogenide case described above, gives rise to a Mott insulating state^{45,46}. The alkaline iron selenides have a “234” phase as well, AFe_{1.5}Se₂, for which too the Mott insulator nature has been suggested based on measurements with angle-resolved photoemission spectroscopy (ARPES)⁴⁷.

C. Orbital-selective Mott physics

To study the effect of electron correlations, it is important to recognize the multi-orbital nature of the electronic states. Conversely, the multi-orbital physics can be utilized to extract clues about the degree and nature of the electron correlations. BaFe₂As₂ is an example of a parent compound, (*i.e.* undoped, stoichiometric) in which the Fe valence is +2. In these compounds, there are $N = 6$ electrons on average that occupy the five 3*d* orbitals of each Fe ion. The theoretical description then is given by multi-orbital Hubbard models, with the minimal interactions being a Hubbard interaction U and a Hund’s coupling J_H . Such models typically include at least the 3*d* *xy* and *xz/yz* orbitals, and can involve all the five 3*d* orbitals. The interplay of the kinetic energy, the short-range repulsion U and the Hund’s

coupling J_H may lead to different behaviors for the various orbitals. It may even be possible that a subset of the orbitals undergoes Mott localization, thus orbital-selective Mott physics.

ARPES measurements have provided evidence^{35,36} for an orbital-selective Mott phase (OSMP). This is illustrated in Fig. 3d, which shows that, for each of the three iron chalcogenides, as temperature goes above about 100 K, the spectral weight for the $3d\ xy$ orbital has vanished, while that for the $3d\ xz/yz$ orbitals has not changed much. The experimental results suggest that this regime can be described by an OSMP, in which the $3d\ xy$ electrons are localized while those associated with the other $3d$ orbitals remain itinerant. Additional evidence for the OSMP has come from THz spectroscopy⁴⁸, Hall measurements⁴⁹, pump-probe spectroscopy⁵⁰ and high-pressure transport measurements⁵¹.

The OSMP was anticipated theoretically. Fig. 3c shows the zero-temperature phase diagram calculated for the potassium iron chalcogenides at the $3d$ -electron filling $N = 6$, in the paramagnetic case with tetragonal lattice symmetry (instead of the AF-ordered case, to highlight the localization effects associated with the Coulomb repulsive interactions). When the combined U and J_H interactions are sufficiently large, a Mott insulator phase arises. An OSMP occurs between this phase and the one in which all the $3d$ orbitals are itinerant.^{40,52} When the electron filling deviates from the commensurate value $N = 6$, the Mott insulator phase is suppressed but the OSMP survives a finite range of electron filling. Similar results arise for a model without the ordered Fe-vacancies.⁴⁰ When the system at zero temperature is purely itinerant but close to the boundary of the OSMP, increasing temperature induces a crossover to an OSMP, which is consistent with experimental observations (Fig. 3d).

Several factors are responsible for the OSMP. First, in the noninteracting limit, the bandwidth of the xy orbital is smaller than those of other orbitals. Second, the Hund's coupling suppresses inter-orbital correlations; this effectively decouples the $3d\ xy$ orbital from others and keeps the xy, xz and yz orbitals effectively at half-filling. (Such an inter-orbital decoupling is also essential for the stability of the OSMP phase, given that the orbitals are mixed in the non-interacting limit.) Third, the degeneracy of the xz and yz orbitals makes the threshold interaction needed for their localization to be larger than its counterpart for the non-degenerate xy orbital¹⁴⁹. As a combined effect of these factors, the $3d\ xy$ orbital has a lower interaction threshold for the Mott transition, and the OSMP ensues. We note that the OSMP is an extreme limit of the effects of orbital-selective correlations. More generally, the $3d\ xy$ orbital is not Mott localized, but is close to a Mott localization,

and the system may still exhibit strong orbital dependent effects^{54–56}. We also note that OSMP is pertinent to other classes of strongly correlated electron systems^{149,150}.

The experimental observations and general considerations summarized in this section suggest the importance of electron-electron correlations in determining the properties of the iron pnictides and chalcogenides. They have provided the basis for various approaches to these systems^{12,14,21,54–67} which are “strong coupling”, in the sense that the effect of electron-electron interactions is treated non-perturbatively.

III. MAGNETISM AND ELECTRONIC NEMATICITY

Because an AF order typically exists near superconductivity in the phase diagram of the FeSCs, magnetism has received considerable attention in the field since the very beginning.⁶⁸ There has also been increasing recognition for the role that nematic order, the breaking of orientational symmetry, plays in uncovering the microscopic physics.

A. Magnetism in the iron pnictides

As already illustrated in Fig. 2b, the parent iron pnictides are antiferromagnetically ordered. The ordering wavevector is $(\pi, 0)$ (the notation is that of the Fe square lattice), as shown in Fig. 4a. This AF order is the background for quantum fluctuations of the spins below the Néel transition temperature T_N . These have been probed by inelastic neutron scattering¹⁵, which measures the frequency and wavevector dependences of the spin structure factor, $S(\mathbf{q}, \omega)$, or of the dynamical spin susceptibility, $\chi''(\mathbf{q}, \omega)$.

A striking feature is that the spin fluctuations remain very strong over a wide temperature range above T_N .^{69–71} In Fig. 4a, the dynamical spin structure factor is shown in terms of equal-intensity contours in the wavevector space. At relatively low energies, these are ellipses near $(\pm\pi, 0)$ and $(0, \pm\pi)$. At high energies, they have the form of spin-wave-like excitations all the way to the boundaries of the AF Brillouin zone⁷⁰. The peak intensity traces out a spin-wave-like energy dispersion, which is also shown in Fig. 4a.

The electron-correlation effects implied by the bad-metal behavior discussed above have inspired the study of the magnetism with the local moments as the starting point. Electron correlations turn the majority of the single-electron excitations incoherent and distribute

them away from the Fermi energy. An expansion has been constructed in terms of the fraction, denoted by w , of the single-electron spectral weight that lies in the low-energy coherent part of the spectrum.^{12,32} To the zeroth order in w , the incoherent electronic excitations (when their charge degrees of freedom are “integrated out”) give rise to localized magnetic moments associated with the Fe ions. In the case of the iron arsenides, the p -orbitals of the As ions mediate the exchange interactions among the local moments. This leads to geometrical frustration in the magnetism: With each As ion sitting at an equal distance from the Fe ions of a square plaquette (Fig. 2a), the exchange interactions contain J_1 and J_2 , between the nearest-neighbor and next-nearest-neighbor sites, respectively, on the Fe-square lattice^{12,72,73}. General considerations suggest that $J_2 > J_1/2$. In this parameter regime, the ground state of the J_1 - J_2 Heisenberg model on the square lattice has the collinear $(\pi, 0)$ order⁷⁴, as is observed experimentally.

Because the charge gap in the incoherent excitations is relatively small, and also due to the Hund’s coupling in the multi-orbital setting⁷⁵ of the Fe-based compounds, multiple spin couplings may be of importance. In particular, the four-spin biquadratic coupling K of the form $K(\mathbf{S}_i \cdot \mathbf{S}_j)^2$ has been shown^{76,77} to be significant. Moreover, at higher order in w , there are itinerant coherent electrons which are coupled to the local moments and introduce damping to the spin excitations. The calculated spin structure factor⁷⁶ for the J_1 - J_2 - K model model in the presence of damping are displayed in Fig. 4b. The theoretical results provide a consistent understanding of the experimental data.

As the majority of the electron spectral weight is in the incoherent sector, the above discussion implies a large spin spectral weight. It has become possible to test this experimentally. In Fig. 4c, χ'' , the momentum-integrated dynamical spin susceptibility⁷⁸ as a function of energy E is shown. A further integration over energy, corresponding to $\int dE \int d\mathbf{q} S(\mathbf{q}, E)$, yields a total spectral weight of about $3\mu_B^2$ per Fe. This corresponds to the spin spectral weight of a full spin-1/2 moment, *i.e.* one μ_B per Fe, as anticipated.

The spin spectral weight and its distribution in energy provide another means to characterize the strength of electron correlations. For weak correlations, the spin degrees of freedom should be described in terms of triplet excitations of electrons and holes near the Fermi energy. In such a weak-coupling description^{79,80}, the enhancement of the spin excitations near $(\pm\pi, 0)$ and $(0, \pm\pi)$ would arise from a Fermi-surface “nesting” effect, *i.e.* the enhanced phase space for connecting the electron and hole Fermi pockets near these

wave vectors. However, the small size of the electron and hole Fermi pockets would limit their contributions to the spin spectral weight to a considerably smaller value than what is observed via the integrated dynamical susceptibility.

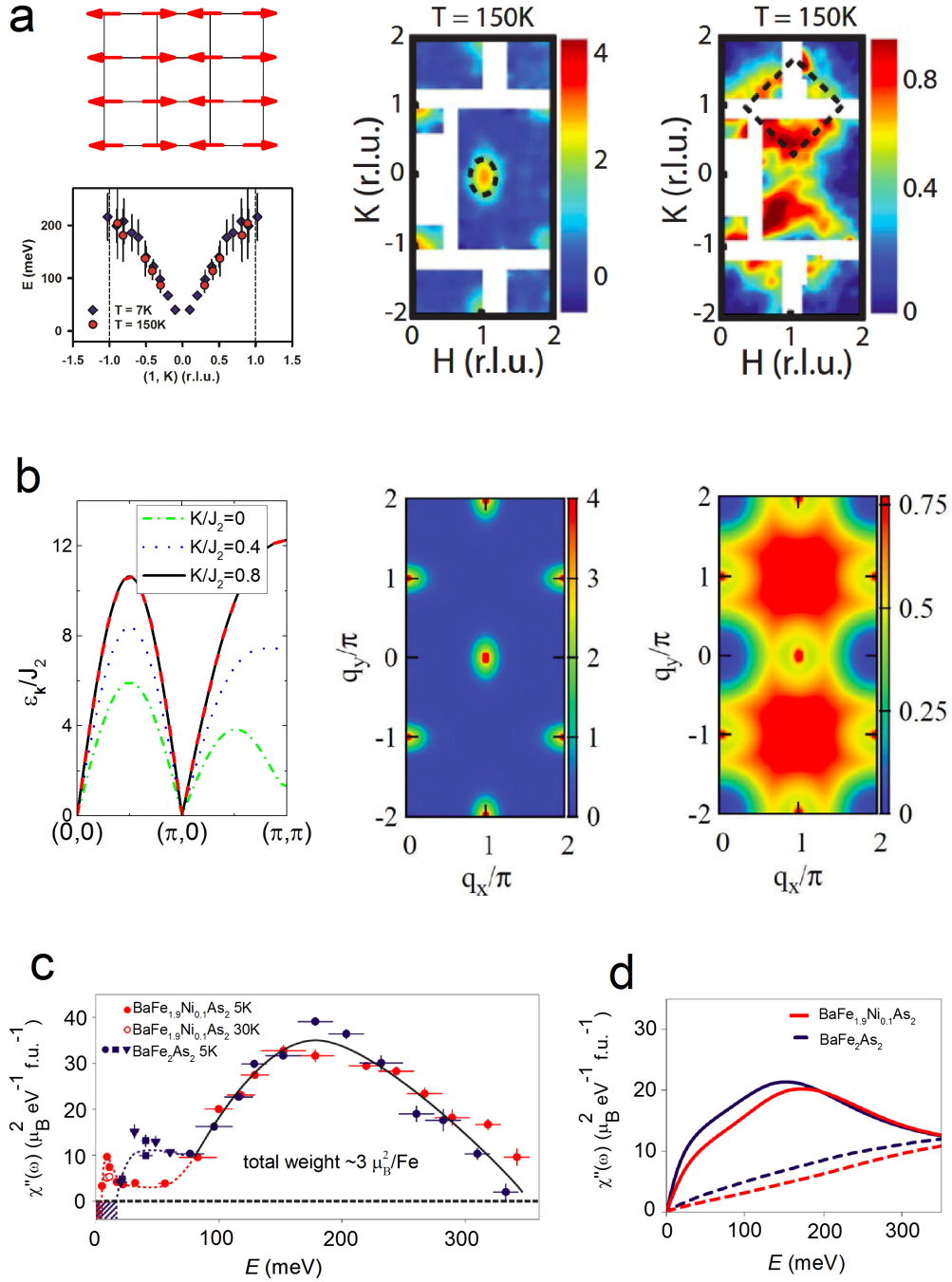


FIG. 4. Magnetism in the iron pnictides. a. Left top panel: the magnetic ordering pattern of the parent iron pnictides such as BaFe_2As_2 . Left bottom, middle and right panels: the energy dispersion and spin structure factor measured in BaFe_2As_2 above the Néel temperature. The wavevector space is denoted by (H,K) (r.l.u.)= $(\text{H}\pi,\text{K}\pi)$ in our notation. Adapted from Ref. 70. b. Theoretically calculated energy dispersion and spin structure factor within a J_1 - J_2 - K model. Adapted from Ref. 76. Also shown are the imaginary part of the dynamical local spin susceptibility measured in pure and Ni-doped BaFe_2As_2 (c) and calculated from the dynamical mean field theory with strong correlations (solid lines) and from the weak-coupling RPA method (dashed lines) (d) adapted from Ref. 78.

A quantitative analysis is shown in Fig. 4d. Calculations based on the dynamical mean-field theory (solid lines), which incorporate the contributions from the incoherent part of the electron spectral weight, capture the right size of the spin spectral weight within the energy range of experimental measurements⁷⁸. A weak-coupling calculation, based on the random-phase approximation (RPA) (dashed lines) considerably underestimates the spin spectral weight.

B. Magnetism in the iron chalcogenides

An AF order also appears in a variety of iron chalcogenides. In FeTe, it has the pattern illustrated in Fig. 5a, corresponding to an ordering wavevector $(\frac{\pi}{2}, \frac{\pi}{2})$. This ordering pattern can be understood in terms of local moments coupled through multi-neighbor J_1 - J_2 - J_3 exchange interactions, in the presence of the biquadratic K couplings^{66,81}. The spin spectral weight, $\int dE \int d\mathbf{q} S(\mathbf{q}, E)$, is now even larger, given that the ordered moment is already $2.5 \mu_B$ per Fe.⁸²

These observations further elucidate the microscopic physics. The Fermi surface in the paramagnetic state of the 11 (*e.g.* FeTe) iron chalcogenides is similar to that of the iron pnictides, as illustrated in Fig. 2c, left panel. For such a Fermi surface, $(\frac{\pi}{2}, \frac{\pi}{2})$ is not a nesting wavevector. Therefore, the magnetic ordering pattern in FeTe cannot be understood within an itinerant nesting description. This suggests that the above considerations on the spin spectral weight of the iron pnictides continue to apply in the FeTe case.

The 245 (*e.g.* $\text{K}_2\text{Fe}_4\text{Se}_5$) alkaline iron selenides have a block spin AF order, as illustrated in Fig. 5c. Again, the ordered moment is large, about $3.3 \mu_B$ per Fe. This magnetic order can be understood in terms of an extended J_1 - J_2 model on a $\frac{1}{5}$ -depleted square lattice with $\sqrt{5} \times \sqrt{5}$ vacancy order^{86,87}. Fig. 5c illustrates the four branches of the observed spin-wave spectra and a theoretical fit based on the local-moment model. The success of this local-moment description of the magnetic dynamics, together with the large ordered moment, provide evidence for the Mott-insulating nature of the 245 alkaline iron selenides. It can also be seen from the momentum distribution of the spin spectral weight^{83,88} that the

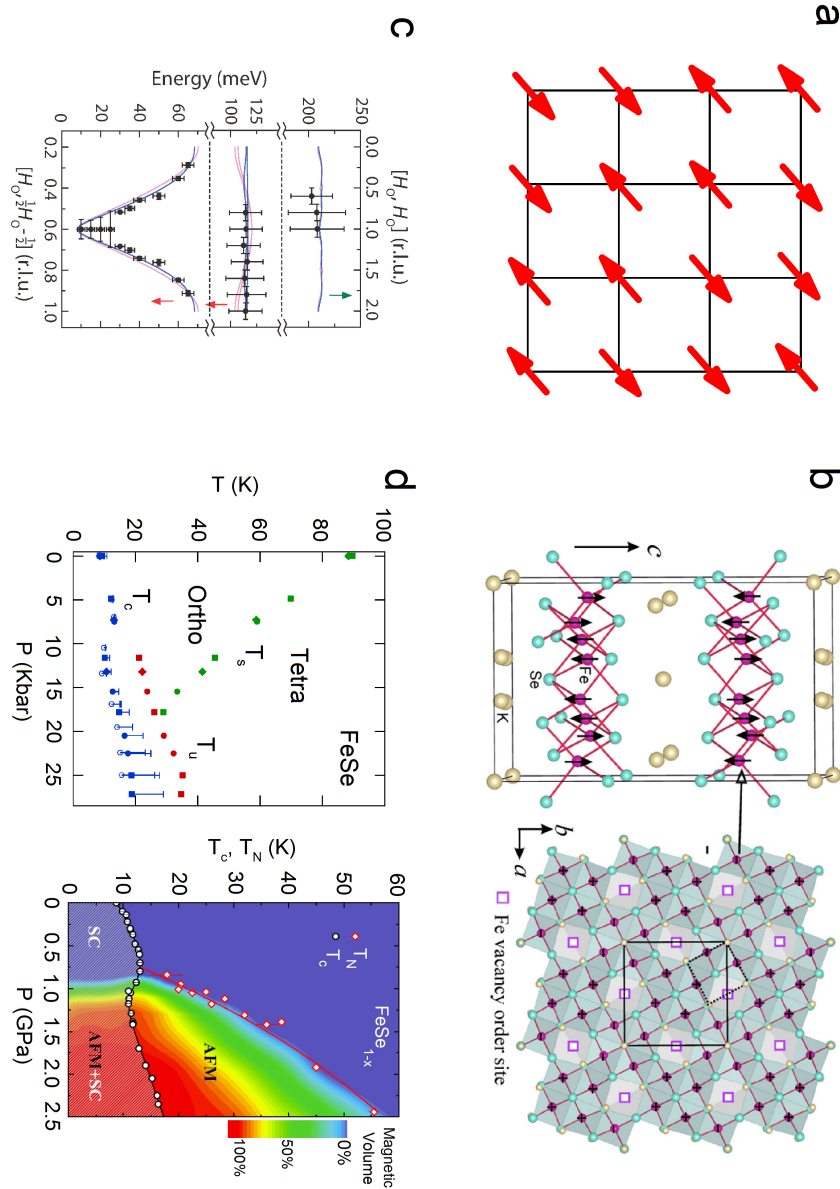


FIG. 5. Magnetism in the iron chalcogenides. a. The magnetic ordering pattern of FeTe. b. The block-spin AF order in the 245 $\text{K}_2\text{Fe}_4\text{Se}_5$ (from Ref. 44) c. The corresponding spin-wave dispersion (from Ref. 83) d. Phase diagram of bulk FeSe, showing the structural transition and pressure-induced superconductivity (left panel, from Ref. 84) and the pressure-induced magnetic order (right panel, from Ref. 85).

damping rate here is smaller than that inferred in the iron pnictides. The overall behavior is similar for the 234 alkaline iron selenides (*e.g.* $\text{Rb}_{0.8}\text{Fe}_{1.6}\text{Se}_2$), but the different vacancy pattern promotes a different AF order⁸⁹.

C. Electronic nematicity and its relation with magnetism

The iron pnictides typically have parent compounds whose ground states have both a collinear $(\pi, 0)$ AF order as well as a structural distortion¹⁵, as illustrated in Fig. 2b. Resistivity anisotropy measurements under uniaxial stress^{16,17} above the structural transition in 122 compounds have revealed a very large electronic nematic response and an examination of the strain dependence of the resistivity anisotropy (proportional to the electronic nematicity) gave compelling evidence that the structural transition is electronically driven. Other probes of the nematic correlations^{145–147}, while not as direct, have given results consistent with that conclusion.

One explanation for the electronic-nematic transition is a magnetic Ising-nematic order. It was recognized from the beginning that models with quasi-local moments and their frustrated Heisenberg J_1 - J_2 interactions¹² feature such an Ising-nematic transition^{18,57,58,74}, and similar conclusions have subsequently been reached in models based on Fermi-surface instabilities⁹¹. While the magnetic mechanism for the nematicity has had considerable success, it is yet to be unequivocally established. An alternative proposal attributes the origin of the nematic order to the orbital degrees of freedom.^{65,92–94} Indeed, ARPES measurements in uniaxially pressurized $\text{BaFe}_{2-x}\text{T}_x\text{As}_2$ show a splitting between the two orthogonal bands, which are otherwise degenerate, that have dominant d_{xz} and d_{yz} characters⁹⁰. Adding to the complication is that symmetry allows a bilinear coupling between the magnetic Ising-nematic and orbital order parameters, and care must be exercised to sharpen the distinction between the scenarios.

Along this direction, two recent developments are worth emphasizing. Neutron scattering experiments have measured the spin-excitation anisotropies^{95,148}. Consider the collinear AF order for the iron pnictides. Applying a uniaxial strain along one axis of the orthorhombic lattice yields a spin excitation anisotropy, as measured by $S_{\text{diff}}(E) \equiv S[(\pi, 0), E] - S[(0, \pi), E]$ in comparison with $S_{\text{sum}}(E) \equiv S[(\pi, 0), E] + S[(0, \pi), E]$. Above the structural transition ($T > T_s$), experiments reveal a strong spin excitation anisotropy in the optimally doped regime, where the ARPES determined splitting between the d_{xz} and d_{yz} bands is already considerably diminished. Moreover quantitatively, while the ARPES-measured orbital splitting energy has gone from about 60 meV in the undoped BaFe₂As₂ to about 20 meV near the optimal electron doping, the energy scale for the spin excitation anisotropy has remained on the order of about 60 meV. These results suggest the dominant role that magnetism plays in leading to the nematic correlations¹⁴⁸.

Another recent development concerns bulk FeSe. As illustrated in Fig. 5d, this compound displays a tetragonal-to-orthorhombic structural transition with $T_s \approx 90$ K, but no Néel transition has been detected^{96–99}. It has been suggested that these results imply a failure of the magnetism-based origin for the structural phase transition^{98,99}. There is, however, a natural way to understand this behavior within the magnetic picture. Several groups have studied the frustrated magnetism associated with the spin-exchange interactions among the local moments^{66,67,100}. Based on the theoretical phase diagram associated with the frustrated bilinear-biquadratic exchange interactions, Ref. 66 proposed that the structural transition in FeSe originates from an Ising-nematic order of an antiferro-quadrupolar phase. This kind of order has the spins preferring an axis without developing an orientation along it, thereby breaking the spin rotational invariance while preserving the time-reversal symmetry. While no static AF order occurs, the collective modes of this quadrupolar state yield $(\pi, 0)$ magnetic fluctuations, which have since been observed by inelastic neutron scattering measurements.^{101,102}

IV. QUANTUM CRITICALITY

In many correlated-electron materials, several ground states can be in competition and it is often possible to tune from one to another through a “quantum critical point” (QCP) by adjusting some control parameter, for example pressure, magnetic field, chemical composi-

tion. An essential characteristic is that dynamical fluctuations of an order parameter play a key role in determining the behavior in the neighborhood of the QCP. Although quantum phase transitions between distinct ground states occur at absolute zero, their effects may be observed over a range of non-zero temperature. The physics of quantum criticality in the iron pnictides and chalcogenides has been reviewed in Ref. 103.

As the iron-based superconductors exhibit a number of different phases: paramagnetic metal, superconductor, antiferromagnet in their phase diagrams, it is reasonable to expect that it is possible to access one or more QCPs by identification of appropriate control parameters. Fig. 6a shows an example, in which the QCP separates an AF metal from a paramagnetic one, and is accessed by a tuning parameter, which, as we discuss below for a particular compound, can be precisely the w of the measure of electron correlations that was introduced in Sec. IIIA.

The considerations of Section II on electronic correlation and proximity to a Mott transition imply that by tuning the ratio of kinetic energy to Coulomb repulsion from small to large, one could pass from an AF state to a paramagnetic one via a magnetic QCP. Fig. 6a is adapted from Ref. 18, where it was first proposed that isoelectronic substitution of P for As in, for example LaFeAsO or BaFe₂As₂, would increase that ratio, here measured by w . This is because P is substantially smaller than As, which leads to a reduction in the unit cell volume (as well as the pnictogen height), thus an increase in kinetic energy.

Apart from its intrinsic interest as an exploratory tool for the physics of quantum criticality, the isoelectronic tuning of w provides a window on the effects of electron correlation that is complementary to the studies described in previous sections, which placed the iron chalcogenides on the side of stronger correlation as compared to the pnictides. Here we move to weaker correlation in the arsenides by P for As substitution.

The proposed phase diagram of Fig. 6a shows a quantum critical region, in which thermodynamic and transport properties are expected to have power-law dependences on temperature and tuning parameter. The ordered phase is an antiferromagnet, which disappears into a paramagnetic Fermi-liquid phase as one passes through the QCP. Crossovers out of the region of quantum criticality are denoted by the dashed red lines. The blue lines represent the thermally-driven AF transition (solid) and an Ising-nematic transition manifested through a structural transition (dashed). The thermal transitions are shown to be two split second-order transitions, but may also be concurrent first-order transitions.

Experimental verification of quantum criticality induced by isoelectronic substitution in order to reduce the correlation effects came soon after the original proposal. This is illustrated in Figs. 6b and 6c. In the former, adapted from Ref. 104, the color shading

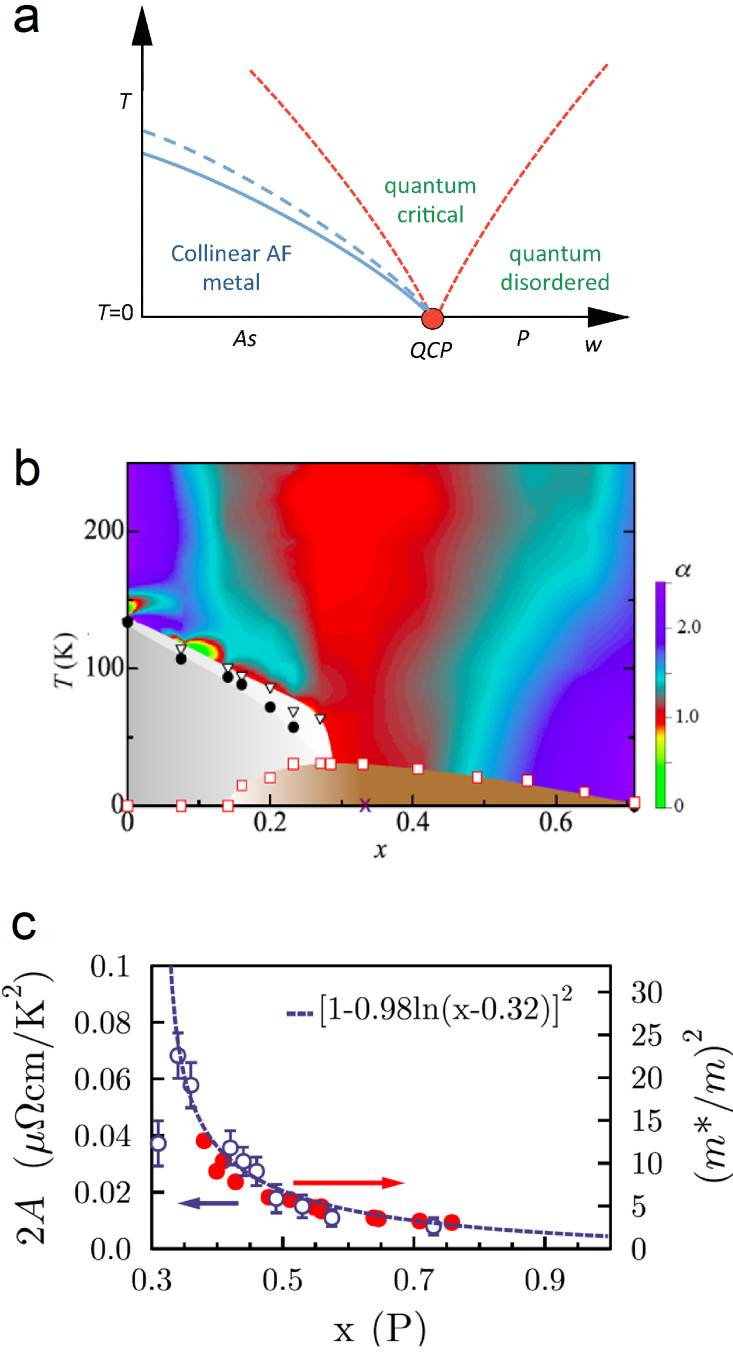


FIG. 6. Quantum criticality in the iron pnictides. a. Quantum criticality in the theoretically proposed phase diagram. The red dot marks a quantum critical point. Adapted from Ref. 18. b. Phase diagram of $\text{BaFe}_2(\text{As}_{1-x}\text{P}_x)_2$. The color shading describes the variation of the resistivity exponent, α , in its temperature dependence, represented by $\rho = \rho_0 + AT^\alpha$. The cross marks the QCP at $x_c = 0.33$. From Ref. 104; courtesy of Y. Matsuda. c. Divergence of m^* , the effective mass, and A , the T^2 -coefficient of the electrical resistivity, on approach of the QCP. Adapted from Ref. 20, containing data of Ref. 107; courtesy of J. Analytis.

represents the resistivity temperature exponent α in $\rho = \rho_0 + AT^\alpha$ in $\text{BaFe}_2(\text{As}_{1-x}\text{P}_x)_2$ (122 compound), in which the QCP occurs at a critical value of $x = x_c \approx 0.33$. The red area indicates the quantum critical regime in which the resistivity has a linear T -dependence as is characteristic¹⁰⁵ for a two-dimensional AF QCP. Furthermore, in the approach to the QCP, the expected singular behavior of thermodynamic quantities is observed as is seen in Fig. 6c, adapted from Ref. 20 which shows the expected¹⁰⁵ logarithmic increase of the electron effective mass as $x \rightarrow x_c$. The left-hand scale shows the measured “ A coefficient” of the T^2 resistivity in the quantum-disordered region, where it should vary as $(m^*)^2$ ¹⁰⁶. This figure demonstrates a consistent quantum critical behavior between transport and thermodynamic measurements *e.g.* specific heat and de Haas-van Alphen data¹⁰⁷.

The use of isoelectronic substitution and its associated quantum criticality is of particular interest in the context of superconductivity: P substitution for As in the Ba 122 compound destroys antiferromagnetism, the grey region in Fig. 6b and enables superconductivity, the brown region in the figure. Although direct access to the QCP is inhibited by the presence of superconductivity, it is observed that as x is varied, the maximum $T_c(x)$ is found very close to $x = x_c$, similarly to what is observed in other strongly-correlated systems.

V. SUPERCONDUCTIVITY DRIVEN BY ANTIFERROMAGNETIC CORRELATIONS

We have thus far discussed that electron correlations in the iron pnictides and chalcogenides are sufficiently strong to place these materials in the bad-metal regime, and that frustrated magnetism of local moments describes the dominant part of the magnetism. What are the implications for unconventional superconductivity? What are the structure and am-

plitude of the superconducting pairing?

The general picture for unconventional superconductivity was illustrated in Fig. 1b. Electron pairs are formed through attractive interactions that are generated while the Coulomb repulsion is being avoided. Pairing correlations will be disfavored between electrons on the same site, which experience the dominant repulsive interactions. Instead, pairing correlations develop among electrons from different sites. Because of this, the orbital part of the pairing wave function tends to be in channels orthogonal to the conventional s -wave channel; these range from an extended s -wave to cases with angular momentum larger than 0.

The proximity of the superconducting phase to the AF ordered phase suggests the importance of the antiferromagnetic correlations for superconductivity. Through the correlation effects implicated by the bad-metal phenomenology and the extensive information about the magnetic ordering and dynamics, we have emphasized the role of frustrating AF exchange interactions. The AF nature of such interactions favors pairing to be in a spin-singlet channel, which is antisymmetric in spin space. Because electrons are fermions, the overall wave function must be antisymmetric under the exchange of electrons. Consequently, the orbital part of the pairing wave function must be symmetric.

A. Superconducting pairing structure and amplitude

A characteristic feature of the iron pnictides and chalcogenides is that the bilinear exchange interactions contain both the nearest-neighbor interaction J_1 and the next-nearest-neighbor interaction J_2 . In particular, we have emphasized the microscopic reasons for the importance of J_2 interaction (see Sec. III.A), which is also supported by the fitting to the spin dynamics measured from neutron scattering experiments. This J_2 interaction favors an extended s -wave pairing function, with the leading term in the wave-vector dependence being $\cos k_x \cos k_y$. In relation to the tetrahedral D_{4h} point group symmetry, this belongs to a pairing state with an A_{1g} symmetry.

For optimally doped iron pnictides, whose Fermi surfaces in the Brillouin zone typically consist of the hole Fermi pockets near the $\Gamma = (0,0)$ point and the electron Fermi pockets near $M = (\pm\pi,0)$ and $(0,\pm\pi)$ points, this extended s -wave gap function is non-zero everywhere on the Fermi surfaces. Moreover, it changes sign across the hole and electron

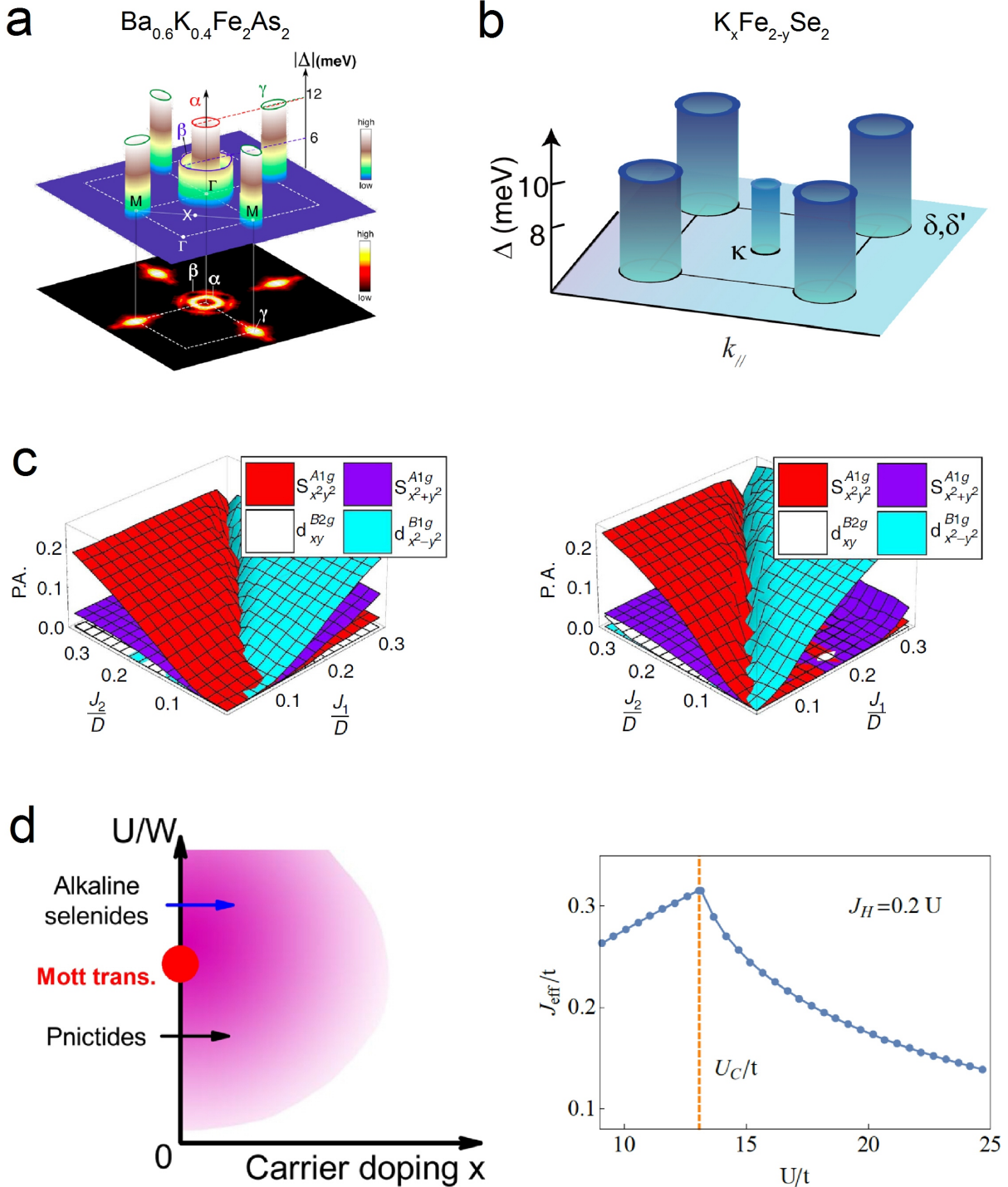


FIG. 7. Superconductivity in the iron pnictides and chalcogenides. Size of the superconducting gap Δ : a. on the hole (α and β) and electron (γ) Fermi pockets in $\text{Ba}_{0.6}\text{K}_{0.4}\text{Fe}_2\text{As}_2$. From Ref. 108; b. on the electron Fermi pockets of dominant (δ and δ') and small (κ) spectral weight, in $\text{K}_x\text{Fe}_{2-y}\text{Se}_2$. From Ref. 109. c. Pairing amplitudes calculated for the iron pnictides and chalcogenides, from Ref. 21. d. Left panel: Schematic phase diagram near a Mott transition. The purple shading marks the parameter regime with strong antiferromagnetic correlations. From Ref. 21. Right panel: Exchange interaction plotted as a function of the Hubbard interaction U , for a Hund's coupling $J_H = 0.2U$ in a two-orbital Hubbard model. From Ref. 110.

pockets. The pairing function is reflected in the single-particle excitation spectrum at the Fermi surface. Where it is nonzero, a gap develops in the spectrum. Where it vanishes, the spectrum is gapless; in other words, there is a node in the gap. ARPES measurements have found a spectrum that is fully gapped. This is shown in Fig. 7a, where the gap function Δ is plotted at the different parts of the Fermi surface; it is seen to have a magnitude of about 10 meV. The ratio $2\Delta/T_c$ is about 4-7, thus larger than the BCS value of ~ 3.5 .

On the other hand, when J_1 is dominant, d -wave pairing with a $(\cos k_x - \cos k_y)$ form factor and a B_{1g} symmetry is favored. In the magnetic frustration regime, with J_2 and J_1 being comparable, a quasi-degeneracy in pairing channels emerges in model calculations. It is interesting that such features arise from a variety of approaches, regardless of whether the correlations are treated non-perturbatively or perturbatively^{21,22,60-63,111-114}.

To distinguish among the various approaches, it is instructive to compare the behavior of the gap in the iron chalcogenides, especially since there are cases when they have only electron Fermi surfaces. This is illustrated in Fig. 7b, for the case of the $\text{K}_x\text{Fe}_{2-y}\text{Se}_2$. We note that, here too, the gap is nodeless. Moreover, the magnitude of the gap for the electron Fermi pockets having the dominant spectral weight (those near the M points in the Brillouin zone) is comparable with that of the iron pnictides. This is consistent with the fact that the superconducting transition temperature (T_c) of $\text{K}_x\text{Fe}_{2-y}\text{Se}_2$ is comparable to that of the iron pnictides.

The lesson of such comparisons is that the pairing amplitudes are comparably large in the cases with or without any hole pocket, that is to say with or without Fermi-surface nesting. This has a natural understanding in models where pairing is driven by short-range

interactions such as the exchange interactions. Fig. 7c shows the pairing amplitude as a function of J_1 and J_2 in multi-orbital models with the pnictide (7c left) and chalcogenide (7c right) -type Fermi surfaces²¹. This shows that, in spite of their distinctive Fermi surfaces, the dominant pairing channels as a function of the exchange interactions are similar in the two cases. Equally important, the pairing amplitudes are comparable in the two cases.

B. Effects of orbital-selectivity on superconducting pairing

As we have discussed in Sec. IIC, electron correlations can show strong orbital selectivity, which affects the electronic properties in the normal states significantly. A natural question is whether the pairing symmetry and amplitudes in the superconducting states are also influenced by the orbital selectivity. Studying this issue provides additional means to explore the effect of electron correlations on the properties of the superconducting state.

Within the strong-coupling approach, the pairing order parameter is defined in the orbital basis and the orbital selectivity can lead to some surprising effects. In the usual case where the dominant pairing is in a full gap s -wave A_{1g} channel, sufficiently strong orbital selectivity may lead to an anisotropic gap along the electron pockets and splitting of spin resonance peaks¹¹⁵. Such effects have been observed in experiments by ARPES¹¹⁶ and neutron scattering^{117,118}, respectively.

A more dramatic case arises in the context of the alkaline iron selenides. As discussed in Sec. V A, in a multiorbital J_1 - J_2 model with orbital independent J_1 and J_2 , the dominant pairing symmetry is either an s -wave A_{1g} channel when J_2 is dominant, or a d -wave B_{1g} channel for dominant J_1 coupling. A recent study¹¹⁹ on this model with orbital dependent J_1 and J_2 reveals that the orbital selectivity plays an essential role in stabilizing an intermediate orbital-selective B_{1g} pairing state that is constructed from the conventional s -wave A_{1g} and d -wave B_{1g} states in the parameter regime where the two are quasi-degenerate. In this orbital-selective B_{1g} pairing state, the dominant pairing amplitude is restricted to the d_{xz} and d_{yz} orbital subspace, in which the pairing state belongs to the B_{1g} representation of the associated point group but has a form factor belonging to the A_{1g} representation due to its nontrivial orbital structure. It is shown that for alkaline iron chalcogenides this pairing state has a full gap, and can produce a spin resonance at wave vector $(\pi, \pi/2)$, which is compatible with both the ARPES and neutron scattering experiments^{109,120–124}.

C. Potential settings for optimizing superconductivity

One grand challenge in physics is whether there is a principle for optimizing superconducting T_c . While superconductivity was initially observed in the iron pnictides with nested hole and electron Fermi pockets, we have already referred to the extensive recent experiments that show that iron chalcogenides with Fermi surface containing only electron pockets exhibit superconductivity of comparable strength. For example, single-layer FeSe on STO substrate has only electron Fermi pockets and, yet, it holds the record of highest T_c in the FeSCs. At the same time, Li(Fe,Co)As with almost perfectly nested Fermi pockets is non-superconducting¹²⁵. These new findings suggest that the Fermi surface geometry plays a secondary role in the superconductivity.

From a theoretical perspective, the pairing amplitudes shown in Fig. 7c for both iron pnictides and alkaline iron selenides may shed some light on this important issue. The results indicate that the pairing amplitudes are proportional to the ratio of J/D , where J is the antiferromagnetic exchange coupling and here and in Fig. 7c, D is the effective bandwidth, as renormalized by electron-electron interactions, whereas W and t in Fig. 7d are the bare bandwidth and kinetic-energy (“hopping”) parameter, respectively.

This result can be generalized to the following principle, which is illustrated in the left panel of Fig. 7d: the maximum of pairing amplitudes, and hence the optimal superconductivity is reached in the parameter regime of the phase diagram near the Mott transition. To see this, we note that, from a recent study on a multiorbital Hubbard model using a slave rotor approach, the exchange interactions increase as the Mott transition is approached from both the insulating and the bad metal sides (right panel of Fig. 7d).¹¹⁰ At the same time, for a system with carrier doping, the renormalized bandwidth D is reduced as the Mott transition is approached by decreasing doping. Correspondingly, at the boundary between electronic localization and delocalization, the ratio J/D will be maximized and so will the superconducting pairing amplitudes. This principle suggests a route for optimizing superconductivity. It also gives an explanation of some key experimental observations, such as the comparable T_c in iron pnictides and alkaline iron selenides, which have very different Fermi surface geometries. In fact, experiments¹⁵ revealed that these two materials have comparable exchange interactions. In addition, both systems can be considered as being in proximity to the point of Mott transition (Fig. 7d, left panel), and therefore have a comparable degree of

bad metallicity and renormalized bandwidth.

VI. DISCUSSION

The subject of the iron-based superconductors is so vast that it does not permit a truly comprehensive survey of manageable length. However, we wish to discuss several additional issues that extend our discussions so far and have the potential for much more in-depth studies.

A. Quantum criticality and emergent phases beyond isoelectronic dopings

The case for quantum criticality is quite strong near the optimal doping under the isoelectronic P-for-As substitution in BaFe_2As_2 , as we have discussed in Sec. IV. By contrast, for carrier-doped iron arsenides, it remains to be established whether the effects of quantum criticality operate near optimal doping over a substantial temperature and energy range. The systems that have been investigated include electron doping associated with Co- or Ni- substitution for Fe, and hole doping induced by K-substitution for Ba. Early evidence came from measurements of the thermopower¹²⁷, nuclear magnetic resonance (NMR)¹²⁸ and ultrasonic attenuation¹²⁹. Measurements based on the electrical transport^{130,131}, neutron scattering¹³², and X-ray scattering¹³³ have revealed the evolution of the transitions towards an AF order as well as a structural order (and the implicated electronic-nematic order) in the Co-doped BaFe_2As_2 ¹³³. The corresponding transition temperatures T_N and T_s gradually decrease with increasing x , which is suggestive of a QCP under the superconducting dome. Precisely how the lines, T_N and T_s *vs.* doping x extrapolate towards the zero-temperature limit, however, has been left open. Indeed, NMR experiments have been interpreted in terms of two separate QCPs, associated with the suppression of the AF and structural transitions, respectively¹³⁴.

This issue has been systematically investigated by neutron and X-ray scattering studies of the structural and magnetic phase transitions in $\text{BaFe}_{2-x}\text{Ni}_x\text{As}_2$.²⁷ The results are consistent with the T_N , for the primary $[(\pi, 0)]$ AF order, and T_s extrapolating towards the same QCP. However, before T_N and T_s can reach zero, the transitions are interrupted by a new magnetic phase, as illustrated in Fig. 2b. The details of this magnetic phase are not yet clear, although

it shows glassy characteristics¹³⁵. Still, the picture that has emerged is that, when the primary magnetic order is sufficiently weakened, other emergent magnetic phases have the chance to appear. In other words, quantum criticality operates over a substantial dynamical range in the form of an “avoided” quantum criticality. The concurrent nature of the quantum criticality associated with the primary AF order and the electronic nematic order appears to have the same form as the quantum criticality predicted for the iso-electronically tuned iron pnictides¹⁸.

Further studies are clearly called for to explore quantum criticality in the carrier-doped iron arsenides. For example, it would be illuminating to investigate the evolution of the low-temperature electrical resistivity as a function of doping x in the normal state induced by suppressing superconductivity by a high magnetic field, as was discussed in Sec. IV for the isoelectronic doping case²⁰. This should be particularly promising, given that the electrical resistivity at optimal Co-doping is quite close to being linear in T ¹⁶. Likewise, ascertaining an E/T scaling in the magnetic and nematic dynamics by neutron scattering would be exceedingly instructive.

B. Connection between iron pnictides and iron chalcogenides

As we already discussed, iron pnictides were the focus of the attention in the beginning of the field. The main families of the iron pnictides, particularly the 1111 and 122 systems, share many similarities in their electronic and magnetic structures: the Fermi surfaces typically consist of nearly nested hole and electron pockets, and the superconductivity is close to a $(\pi, 0)$ collinear AF order in the phase diagram. Subsequently, the iron chalcogenides were extensively studied. These systems show considerable variance in their electronic and magnetic properties: some high T_c compounds have only electron pockets, and the AF ground state could be considerably different from the $(\pi, 0)$ AF order.

We have taken the perspective that most of the iron pnictides and essentially all the chalcogenides have an electron occupancy on the $3d$ orbitals that is close to 6, and the degree of electronic correlations forms a continuum from the iron phosphides through iron arsenides all the way to the iron chalcogenides. A unified phase diagram is illustrated by the results of theoretical studies on the correlation effects – of both the direct Coulomb repulsion U and the Hund’s coupling J_H – in multi-orbital Hubbard models, similar to the one shown

in the left panel of Fig.3c.^{40,52,54} This is consistent with the fact, as already discussed in Sec.IIA, that both iron pnictides and iron chalcogenides show bad metal behavior in their normal states. It is also compatible with the results of dynamical mean-field studies in a variety of iron pnictides and chalcogenides¹⁴. Along this line of consideration, a physical pathway may be constructed to connect the insulating 245 alkaline iron selenides with their superconducting counterparts^{40,51}, providing the basis for the placement of these materials in the illustrative phase diagram shown in Fig. 7c, left panel.

What would be particularly instructive is to realize materials system in which the degree of electronic correlations, including orbital selectivity, can be continuously tuned. Progress along this direction has recently become possible. For example, recent experiments have revealed the intriguing effect of tuning the S-for-Se and Te-for-Se substitution series^{126,136} in the alkaline iron chalcogenides. S-doping introduces negative chemical potential and leads to an enhanced kinetic energy, effectively reducing the strength of electron correlations. By contrast, Te-doping enhances correlation effects and moves the system towards an insulating ground state.

C. Extremely hole doped $A\text{Fe}_2\text{As}_2$ iron pnictides

Yet another way to tune the system is to vary the $3d$ -electron filling such that it reaches far away from $N = 6$. The alkali iron pnictides $A\text{Fe}_2\text{As}_2$ with $A = \text{K}, \text{Rb},$ and Cs provide an opportunity to study such effects. Valence counting gives $N = 5.5$ for these systems, corresponding to a large hole doping relative to the usual parent iron arsenides. This is verified by ARPES experiments, which show that the Fermi surfaces in these compounds contain only hole pockets²⁹. Even though their superconducting transition temperature T_c is small (3.5 K in the case $A = \text{K}$, and becomes even smaller for the Rb and Cs cases), experimental evidence suggests that the superconductivity is unconventional¹³⁷⁻¹⁴⁰. Moreover, there is a huge mass enhancement implying that they are strongly correlated¹⁴¹⁻¹⁴³.

The fact that $A\text{Fe}_2\text{As}_2$ is in between the $N = 6$ and $N = 5$ limits suggests that studying this system may link the properties of the usual systems close to $N = 6$ with those closer to $N = 5$. If all the five $3d$ orbitals were degenerate, $N = 5$ would correspond to half filling, while $N = 6$ would be considerably away from half filling. However, the $3d$ orbitals in these systems are non-degenerate, and we have discussed in Sec. II C that, even for $N = 6$, the $3d$

xy , xz and yz orbitals can be close to half filling over an extended range of electron-electron interactions. Studying the orbital selectivity as N goes from 6 to 5 would therefore help reveal the nature of the electron correlations in the iron pnictides^{52,55}.

This issue is actively being studied experimentally. There is evidence that a particular orbital (the d_{xy} orbital, for example) is closer to Mott localization. In other words, the system may be closer to an orbital-selective Mott transition. The particularly enhanced correlations in the nearly localized orbital explain the unusually large Sommerfeld coefficients observed experimentally, while measurement of the Grüneisen ratio suggests a proximity to quantum criticality as A goes from K through Rb to Cs¹⁴³. It will be illuminating to understand the nature of this QCP and its detailed relationship to superconductivity, as well as to explore how to extend N from 5.5 towards 5¹⁴³.

VII. SUMMARY AND OUTLOOK

Concerted efforts during the past seven years have led to a large materials basis for superconductivity in the iron pnictides and chalcogenides. The superconducting transition temperatures are high compared to those of conventional superconductors and in the bulk materials at ambient pressure are second only to those achieved in the copper oxides. Moreover, recent experiments have shown that T_c can be further increased in the iron chalcogenides.

The microscopic physics and superconductivity of the iron pnictides and chalcogenides is the subject of active ongoing studies, both theoretical and experimental. Still, extensive understandings have already been achieved, which we have summarized. These include:

- The normal state of the iron-based superconductors is a bad metal. More specifically, the DC electrical resistivity at room temperature is large, reaching the Mott-Ioffe-Regel limit. Relatedly, the Drude weight of the optical conductivity is strongly suppressed compared to its non-interacting counterpart. A relatively modest enhancement of the electron-correlation strength through a kinetic-energy reduction leads to a fully localized, Mott-insulating regime. These and other properties provide compelling evidence that the iron pnictides and chalcogenides are strongly correlated in that the effect of electron correlations is non-perturbative. They also provide evidence for the normal state being in proximity to a Mott transition. Relatedly, orbital selectivity has been

found in the bad-metal regime, with its extreme form being an orbital-selective Mott phase.

- The spin excitations map out a spin-wave-like spectrum. The total spectral weight of the observed excitations is large, in that it corresponds to a local moment on the order of one to several μ_B per Fe. Across the materials basis, the variation in the size of the local moments goes well with the variation in the degree of electron correlations inferred from electrical transport and charge dynamics studies. The energy dispersions of the spin excitations implicate a J_1 - J_2 magnetic frustration, as was theoretically recognized from the beginning of the field. The detailed energy and momentum distributions of the spin spectral weight encode the damping of the spin excitations, whose variation across the materials basis also seems consistent with the corresponding variation in the degree of electron correlations.
- Electronic nematicity has been observed in the normal state of many if not all the FeSCs. There is considerable evidence that its origin lies in the spin degrees of freedom, although the issue remains to be fully settled.
- Compelling experimental evidence has accumulated for quantum criticality predicted to occur in the isoelectronic P-doped iron arsenides. There is also indication for quantum criticality in the carrier-doped iron arsenides, although the case here needs to be further substantiated.
- Superconductivity is unconventional in that it is primarily driven by electron-electron interactions and, relatedly, that the superconducting pairing is not in the conventional s -wave channel. We have summarized the arguments for superconductivity being primarily driven by antiferromagnetic correlations, and discussed the implications of the comparably large T_c and pairing amplitudes observed in the FeSCs with or without a Fermi-surface nesting. Finally, there is considerable theoretical basis for the quasi-degeneracy among several competing channels of superconducting pairing.

The properties observed in these materials and the theoretical considerations outlined here suggest that optimized superconductivity occurs in bad metals that are not only close to a magnetic order but also at the boundary of electronic localization and delocalization. This notion connects the FeSCs to unconventional superconductivity that has been observed in

other classes of strongly correlated materials, such as the copper oxides, heavy fermion metals and organic charge-transfer salts. Indeed, the normal state of all these other superconductors satisfies the criterion of bad metals. Therefore, higher T_c superconductivity may appear in materials which possess even larger antiferromagnetic exchange interactions but retain bad metallicity.

Acknowledgments We would like to thank J. Analytis, M. Bendele, P. C. Dai, W. Ding, L. Harriger, X. Lu and P. Nikolic for their helpful input on the manuscript. We have benefited from collaborations and/or discussions with J. Dai, P. C. Dai, W. Ding, P. Goswami, K. Grube, D. H. Lu, A. H. Nevidomskyy, E. Nica, P. Nikolic, Z.-X. Shen, H. von Löhneysen, Z. Wang, M. Yi, and J.-X. Zhu. The work has been supported in part by the NSF Grant No. DMR-1309531 and the Robert A. Welch Foundation Grant No. C-1411 (Q.S.), and by the National Science Foundation of China Grant number 11374361 and the Fundamental Research Funds for the Central Universities and the Research Funds of Renmin University of China (R.Y.). We acknowledge the support provided in part by the NSF Grant No. NSF PHY11-25915 at KITP, UCSB, for our participation in the Fall 2014 program on “Magnetism, Bad Metals and Superconductivity: Iron Pnictides and Beyond”. Q.S. and E.A. also acknowledge the hospitality of the Aspen Center for Physics (NSF Grant No. 1066293).

-
1. Kamihara, Y., Watanabe, T., Hirano, M. & Hosono, H. Iron-Based Layered Superconductor La[O_{1-x}F_x]FeAs ($x = 0.05-0.12$) with $T_c = 26$ K. *J. Am. Chem. Soc.* **130**, 3296 (2008).
 2. Bednorz, J. G., Müller, K. A. Possible High T_c Superconductivity in the Ba- La-Cu-O System. *Z. Phys. B- Condensed Matter* **64**, 189 (1986).
 3. Ren Z. A. *et al.*, Superconductivity at 55K in Iron-Based F-Doped Layered Quaternary Compound Sm[O_{1-x}F_x]FeAs. *Chin. Phys. Lett.* **25**, 2215 (2008).
 4. Wang, Q.-Y. *et al.* Interface-Induced High-Temperature Superconductivity in Single Unit-Cell FeSe Films on SrTiO₃. *Chin. Phys. Lett.* **29**, 037402 (2012).
 5. He, S. *et al.* Phase Diagram and High Temperature Superconductivity at 65 K in Tuning Carrier Concentration of Single-Layer FeSe Films. *Nat. Mater.* **12**, 605 (2013).
 6. Lee, J. J. *et al.* Interfacial mode coupling as the origin of the enhancement of T_c in FeSe films

- on SrTiO₃. *Nature* **515**, 245-248 (2014).
7. Zhang, Z. *et al.* Onset of the Meissner effect at 65 K in FeSe thin film grown on Nb doped SrTiO₃ substrate. *Science Bulletin* **60**, 1301-1304 (2015).
 8. Ge, J.-F., *et al.*, Superconductivity above 100 K in single-layer FeSe films on doped SrTiO₃. *Nat. Mater.* **14**, 285 (2015).
 9. Kamerlingh Onnes, H. *Commun. Phys. Lab. Univ. Leiden. Suppl.* **29** (1911).
 10. Bardeen, J., Cooper, L. & Schrieffer, J.R. Microscopic Theory of Superconductivity. *Phys. Rev.* **106**, 162 (1957).
 11. Boeri, L., Dolgov, O. V. & Golubov, A. A. Is LaFeAsO_{1-x}F_x an Electron-Phonon Superconductor? *Phys. Rev. Lett.* **101**, 026403 (2008).
 12. Si, Q. & Abrahams, E. Strong Correlations and Magnetic Frustration in the High T_c Iron Pnictides. *Phys. Rev. Lett.* **101**, 076401 (2008)
 13. Qazilbash, M.M. *et al* Electronic correlations in the iron pnictides *Nature Physics* **5**. 647 (2009).
 14. Yin, Z. P., Haule, K. & Kotliar, G. Kinetic frustration and the nature of the magnetic and paramagnetic states in iron pnictides and iron chalcogenides. *Nature Mater.* **10**, 932 (2011).
 15. Dai, P. C. Antiferromagnetic order and spin dynamics in iron-based superconductors. *Rev. Mod. Phys.* **87**, 855 (2015).
 16. Chu, J. H., Kuo, H.-H., Analytis, J. G. & Fisher, I. R. Divergent Nematic Susceptibility in an Iron Arsenide Superconductor. *Science* **337**, 710-712 (2012).
 17. Kuo, H.-H., Chu, J. -H., Kivelson, S. A. & Fisher, I. R. Ubiquitous signatures of nematic quantum criticality in optimally doped Fe-based superconductors. *arXiv:1503.00402v1*.
 18. J. Dai, Q. Si, J.-X. Zhu, and E. Abrahams, Iron pnictides as a new setting for quantum criticality. *Proc. Natl. Acad. Sci. USA* **106**, 4118 - 4121 (2009).
 19. Hashimoto, K. *et al.* A Sharp Peak of the Zero-Temperature Penetration Depth at Optimal Composition in BaFe₂(As_{1-x}P_x)₂. *Science* **336**, 1554 (2012).
 20. Analytis, J.G. *et al.* Transport near a quantum critical point in BaFe₂(As_{1-x}P_x)₂. *Nature Phys.* **10**, 194 (2014).
 21. Yu, R., Goswami, P., Si, Q. Nikolic, P., and Zhu, J.-X. Superconductivity at the Border of Electron Localization and Itinerancy. *Nat. Commun.* **4**, 2783 (2013).
 22. Hirschfeld, P. J., Korshunov, M. M. and Mazin, I. I. Gap symmetry and structure of Fe-based

- superconductors. *Rep. Prog. Phys.* **74**, 124508 (2011).
23. Rotter, M., Tegel, M. & Johrendt, D. Superconductivity at 38K in the Iron Arsenide $(\text{Ba}_{1-x}\text{K}_x)\text{Fe}_2\text{As}_2$. *Phys. Rev. Lett.* **101**, 107006 (2008).
 24. Hsu, F.-C. *et al.* Superconductivity in the PbO-type structure α -FeSe. *Proc. Natl. Acad. Sci. USA* **105**, 14262 (2008).
 25. Guo, J. *et al.* Superconductivity in the iron selenide $\text{K}_x\text{Fe}_2\text{Se}_2$ ($0 \leq x \leq 1.0$). *Phys. Rev. B* **82**, 180520 (2010).
 26. Sun, L. *et al.* Re-emerging superconductivity at 48 Kelvin in iron chalcogenides. *Nature* **483**, 67-69 (2012).
 27. Lu X. *et al.* Avoided quantum criticality and magnetoelastic coupling in $\text{BaFe}_{2-x}\text{Ni}_x\text{As}_2$. *Phys. Rev. Lett.* **110**, 257001 (2013).
 28. Yi, M. *et al.* Electronic Structure of the BaFe_2As_2 Family of Iron Pnictides. *Phys. Rev. B* **80**, 024515 (2009).
 29. Sato, T. *et al.* Band Structure and Fermi Surface of an Extremely Overdoped Iron-Based Superconductor KFe_2As_2 . *Phys. Rev. Lett.* **103**, 047002 (2009).
 30. Hussey, N. E., Takenaka, K., and Takagi, H. Universality of the Mott-Ioffe-Regel limit in metals. *Philos. Mag.* **84**, 2847 (2004).
 31. Fawcett, E. Spin-density-wave antiferromagnetism in chromium *Rev. Mod. Phys.* **60**, 209(1988).
 32. Si, Q., Abrahams, E., Dai, J. & Zhu, J.-X. Correlation effects in the iron pnictides. *New Journal of Physics* **11**, 045001 (2009).
 33. M. Nakajima *et al.* Normal-state charge dynamics in doped BaFe_2As_2 : Roles of doping and necessary ingredients for superconductivity. *Sci. Rep.* **4**, 5873 (2014).
 34. Tamai, A. *et al.* Strong electron correlations in the normal state of the iron-based $\text{FeSe}_{0.42}\text{Te}_{0.58}$ superconductor observed by angle-resolved photoemission spectroscopy. *Phys. Rev. Lett.* **104**, 097002 (2010).
 35. Yi, M. *et al.* Observation of temperature-induced crossover to an orbital-selective Mott phase in $\text{A}_x\text{Fe}_{2-y}\text{Se}_2$ (A=K, Rb) superconductors. *Phys. Rev. Lett.* **110**, 067003 (2013).
 36. Yi, M. *et al.* Observation of universal strong orbital-dependent correlation effects in iron chalcogenides. *Nature Commun.* **6**, 7777 (2015).
 37. Si, Q. Iron pnictide superconductors: Electrons on the verge. *Nat. Phys.* **5**, 629 (2009).

38. Zhu, J.-X. *et al.* Band narrowing and Mott localization in iron oxychalcogenides $\text{La}_2\text{O}_2\text{Fe}_2\text{O}(\text{Se,S})_2$. *Phys. Rev. Lett.* **104**, 216405 (2010).
39. Fang, M.-H. *et al.* Fe-based superconductivity with $T_c = 31$ K bordering an antiferromagnetic insulator in $(\text{Tl,K})\text{Fe}_x\text{Se}_2$. *Europhys. Lett.* **94**, 27009 (2011).
40. Yu R. & Si Q. Orbital-selective Mott phase in multiorbital models for alkaline iron selenides $\text{K}_{1-x}\text{Fe}_{2-y}\text{Se}_2$. *Phys. Rev. Lett.* **110**, 146402 (2013).
41. Free, D. G. & Evans, J. S. O. Low-temperature nuclear and magnetic structures of $\text{La}_2\text{O}_2\text{Fe}_2\text{OSe}_2$ from x-ray and neutron diffraction measurements. *Phys. Rev. B* **81**, 214433 (2010).
42. Imada, M., Fujimori, A. & Tokura, Y. Metal-insulator transitions. *Rev. Mod. Phys.* **70**, 1039 (1998).
43. Freelon, B. *et al.* Mott-Kondo Insulator Behavior in the Iron Oxychalcogenides. arXiv:1501.00332.
44. Bao, W. *et al.* A Novel Large Moment Antiferromagnetic Order in $\text{K}_{0.8}\text{Fe}_{1.6}\text{Se}_2$ Superconductor. *Chin. Phys. Lett.* **28**, 086104 (2011).
45. Yu, R., Zhu, J.-X. & Si, Q. Mott transition in Modulated Lattices and Parent Insulator of $(\text{K, Tl})_y\text{Fe}_x\text{Se}_2$ Superconductors. *Phys. Rev. Lett.* **106**, 186401 (2011).
46. Zhou, Y., Xu, D.-H., Zhang, F.-C. & Chen, W.-Q. Theory for superconductivity in $(\text{Tl,K})\text{Fe}_x\text{Se}_2$ as a doped Mott insulator. *EuroPhys. Lett.* **95**, 17003 (2011).
47. Wang, M. *et al.* Mott localization in a pure stripe antiferromagnet $\text{Rb}_{1-\delta}\text{Fe}_{1.5-\sigma}\text{S}_2$. *Phys. Rev. B* **92**, 121101 (2015)
48. Wang, Z. *et al.* Orbital-selective metal-insulator transition and gap formation above T_c in superconducting $\text{Rb}(1-x)\text{Fe}(2-y)\text{Se}_2$. *Nat. Commun.* **5**, 3202 (2014).
49. Ding, X., Pan, Y., Yang, H. & Wen, H.-H. Strong and nonmonotonic temperature dependence of Hall coefficient in superconducting $\text{K}_x\text{Fe}_{2-y}\text{Se}_2$ single crystals. *Phys. Rev. B* **89**, 224515 (2014).
50. Li, W. *et al.* Mott behaviour in $\text{K}_x\text{Fe}_{2-y}\text{Se}_2$ superconductors studied by pump-probe spectroscopy. *Phys. Rev. B* **89**, 134515 (2014).
51. Gao, P. *et al.* Role of the 245 phase in alkaline iron selenide superconductors revealed by high-pressure studies. *Phys. Rev. B* **89**, 094514 (2014).
52. Yu R., Zhu J.-X. & Si Q. Orbital-dependent effects of electron correlations in microscopic

- models for iron-based superconductors. *Current Opinion in Solid State and Materials Science* **17**, 65-71 (2013).
53. Anisimov, V. I., Nekrasov, I. A., Kondakov, D. E., Rice, T. M. & Sigrist, M. Orbital-selective Mott-insulator transition in $\text{Ca}_{2-x}\text{Sr}_x\text{RuO}_4$. *Eur. Phys. J. B* **25**, 191 (2002).
 54. Yu, R. & Si, Q. $U(1)$ Slave-spin theory and its application to Mott transition in a multi-orbital model for iron pnictides. *Phys. Rev. B* **86**, 085104 (2012)
 55. de'Medici, L., Giovannetti, G. & Capone, M. Selective Mottness as a key to iron superconductors. *Phys. Rev. Lett.* **112**, 177001 (2014).
 56. Bascones, E., Valenzuela, B. & Calderón, M. J. Orbital differentiation and the role of orbital ordering in the magnetic state of Fe superconductors. *Phys. Rev. B* **86**, 174508 (2012).
 57. Fang, C., Yao, H., Tsai, W.-F., Hu, J. P., and Kivelson, S. A. Theory of electron nematic order in LaFeAsO , *Phys. Rev. B* **77**, 224509 (2008).
 58. Xu, C., Muller, M., and Sachdev, S. Ising and spin orders in the iron-based superconductors, *Phys. Rev. B* **78**, 020501(R) (2008).
 59. Laad, M. S., Craco, L., Leoni, S. & Rosner, H. Electrodynamic response of incoherent metals: Normal phase of iron pnictides. *Phys. Rev. B* **79** 024515 (2009).
 60. Seo, K., Bernevig, B. A. & Hu, J. Pairing Symmetry in a Two-Orbital Exchange Coupling Model of Oxypnictides. *Phys. Rev. Lett.* **101**, 206404 (2008).
 61. Moreo, A., Daghofer, M., Riera, J. A. & Dagotto, E. Properties of a two-orbital model for oxypnictide superconductors: Magnetic order, B_{2g} spin-singlet pairing channel, and its nodal structure *Phys. Rev. B* **79**, 134502 (2009).
 62. Chen, W.-Q., Yang, K.-Y., Zhou, Y., and Zhang, F.-C. Strong Coupling Theory for Superconducting Iron Pnictides. *Phys. Rev. Lett.* **102**, 047006 (2009).
 63. Yang, F., Wang, F., and Lee, D.-H. Fermiology, orbital order, orbital fluctuations, and Cooper pairing in iron-based superconductors. *Phys. Rev. B* **88**, 100504 (R) (2013).
 64. Berg, E., Kivelson, S. A. & Scalapino, D. J. A twisted ladder: relating the Fe superconductors to the high- T_c cuprates. *New J. Phys.* **11**, 085007 (2009).
 65. Lv, W., Krüger, F., and Phillips, P. Orbital ordering and unfrustrated $(\pi,0)$ magnetism from degenerate double exchange in the iron pnictides. *Phys. Rev. B* **82**, 045125 (2010).
 66. Yu, R. & Si, Q. Antiferroquadrupolar and Ising-nematic orders of a frustrated bilinear-biquadratic Heisenberg model and implications for the magnetism of FeSe . *Phys. Rev. Lett.*

- 115**, 116401 (2015).
67. Wang, F., Kivelson, S. A. & Lee, D.-H. Nematicity and quantum paramagnetism in FeSe. *Nature Phys.* (2015); online at doi:10.1038/nphys3456.
 68. de la Cruz, C. *et al.* Magnetic Order versus superconductivity in the Iron-based layered $\text{La}(\text{O}_{1-x}\text{F}_x)\text{FeAs}$ systems. *Nature* **453**, 899 (2008).
 69. Diallo, S. O. *et al.* Paramagnetic spin correlations in CaFe_2As_2 single crystals. *Phys. Rev. B* **81**, 214407 (2010).
 70. Harriger, L. W. *et al.* Nematic spin fluid in the tetragonal phase of BaFe_2As_2 . *Phys. Rev. B* **84**, 054544 (2011).
 71. Ewings, R. A. *et al.* Itinerant spin excitations in SrFe_2As_2 measured by inelastic neutron scattering. *Phys. Rev. B* **83**, 214519 (2011).
 72. Yildirim, T. Origin of the 150-K Anomaly in LaFeAsO : Competing antiferromagnetic interactions, frustration, and a structural phase transition. *Phys. Rev. Lett.* **101**, 057010 (2008).
 73. Ma, F., Lu, Z.-Y. & Xiang, T. Antiferromagnetic superexchange interactions in LaOFeAs . *Phys. Rev. B* **78**, 224517 (2008).
 74. Chandra, P., Coleman, P. & Larkin, A. I. Ising transition in frustrated Heisenberg models. *Phys. Rev. Lett.* **64**, 88-91 (1990).
 75. Fazekas, P. *Lecture Notes on Electron Correlation and Magnetism* (World Scientific, Singapore, 1999), Chap. 5.
 76. Yu, R. *et al.* Spin dynamics of a $J_1 - J_2 - K$ model for the paramagnetic phase of iron pnictides. *Phys. Rev. B* **86**, 085148 (2012)
 77. Wysocki, A. L., Belashchenko, K. D. & Antropov, V. P. Consistent model of magnetism in ferropnictides. *Nature Phys.* **7**, 485 (2011).
 78. Liu, M. S. *et al.* Nature of magnetic excitations in superconducting $\text{BaFe}_{1.9}\text{Ni}_{0.1}\text{As}_2$. *Nat. Phys.* **8**, 376-381 (2012).
 79. Dong, J. *et al.* Competing orders and spin-density-wave instability in $\text{La}(\text{O}_{1-x}\text{F}_x)\text{FeAs}$. *Europhys. Lett.* **83**, 27006 (2008).
 80. Knolle, J., Eremin, I. & Moessner, R. Multiorbital spin susceptibility in a magnetically ordered state: Orbital versus excitonic spin density wave scenario. *Phys. Rev. B* **83**, 224503 (2011).
 81. Ma, F., Ji, W., Hu, J., Lu, Z.-Y. and Xiang, T. First-Principles Calculations of the Electronic Structure of Tetragonal α -FeTe and α -FeSe Crystals: Evidence for a Bicollinear Antiferro-

- magnetic Order. *Phys. Rev. Lett.* **102**, 177003 (2009).
82. Wen, J. Magnetic neutron scattering studies on the Fe-based superconductor system $\text{Fe}_{1+y}\text{Te}_{1-x}\text{Se}_x$. *Annals Phys.* **358**, 92 (2015).
 83. Wang, M. *et al.* Spin waves and magnetic exchange interactions in insulating $\text{Rb}_{0.89}\text{Fe}_{1.58}\text{Se}_2$. *Nat. Commun.* **2**, 580 (2011).
 84. Terashima, T. *et al.* Pressure-Induced Antiferromagnetic Transition and Phase Diagram in FeSe . *J. Phys. Soc. Jpn.* **84**, 063701 (2015).
 85. Bendele, M. *et al.* Coexistence of superconductivity and magnetism in FeSe_{1-x} under pressure. *Phys. Rev. B* **85**, 064517 (2012).
 86. Yu, R., Goswami, P. & Si, Q. The magnetic phase diagram of an extended J_1 - J_2 model on a modulated square lattice and its implications for the antiferromagnetic phase of $\text{K}_y\text{Fe}_x\text{Se}_2$. *Phys. Rev. B* **84**, 094451 (2011).
 87. Cao, C. & Dai, J. Block Spin Ground State and Three-Dimensionality of $(\text{K,Tl})\text{Fe}_{1.6}\text{Se}_2$. *Phys. Rev. Lett.* **107**, 056401 (2011).
 88. Chi, S. *et al.* Neutron scattering study of spin dynamics in superconducting $(\text{Tl,Rb})_2\text{Fe}_4\text{Se}_5$. *Phys. Rev. B* **87**, 100501 (2013).
 89. Wang, M. *et al.* Two spatially separated phases in semiconducting $\text{Rb}_{0.8}\text{Fe}_{1.5}\text{S}_2$. *Phys. Rev. B* **90**, 125148 (2014).
 90. Yi, M. *et al.* Symmetry breaking orbital anisotropy on detwinned $\text{Ba}(\text{Fe}_{1-x}\text{Co}_x)_2\text{As}_2$ above the spin density wave transition. *Proc. Natl. Acad. Sci. USA* **108**, 6878 (2011).
 91. Fernandes, R. M., Chubukov, A. V., and Schmalian, J. Nematic order in iron superconductors - who is in the driver's seat? *Nat. Phys.* **10**, 97 (2014).
 92. Chen, C.-C. *et al.* Orbital Order and Spontaneous Orthorhombicity in Iron Pnictides. *Phys. Rev. B* **82**, 100504(R) (2010).
 93. Lee, C. C., Yin, W. G. & Ku, W. Ferro-Orbital Order and Strong Magnetic Anisotropy in the Parent Compounds of Iron-Pnictide Superconductors. *Phys. Rev. Lett.* **103**, 267001 (2009).
 94. Krüger, F., Kumar, S., Zaanen, J., and van den Brink, J. Spin-orbital frustrations and anomalous metallic state in iron-pnictide superconductors. *Phys. Rev. B* **79**, 054504 (2009).
 95. Lu, X. *et al.* Nematic spin correlations in the tetragonal state of uniaxial strained $\text{BaFe}_{2-x}\text{Ni}_x\text{As}_2$. *Science* **345**, 657-660 (2014).
 96. McQueen, T. M. *et al.* Tetragonal-to-Orthorhombic Structural Phase Transition at 90 K in

- the Superconductor $\text{Fe}_{1.01}\text{Se}$. *Phys. Rev. Lett.* **103**, 057002 (2009).
97. Medvedev, S. *et al.* Electronic and magnetic phase diagram of $\beta\text{-Fe}_{1.01}\text{Se}$ with superconductivity at 36.7 K under pressure. *Nat. Mater.* **8**, 630 (2009).
 98. Böhmer, A. E. *et al.* Origin of the Tetragonal-to-Orthorhombic Phase Transition in FeSe: A Combined Thermodynamic and NMR Study of Nematicity. *Phys. Rev. Lett.* **114**, 027001 (2015).
 99. Baek, S.-H. *et al.* Orbital-driven nematicity in FeSe. *Nat. Mater.* **14**, 210 (2015).
 100. Glasbrenner J. K. *et al.* Effect of magnetic frustration on nematicity and superconductivity in iron chalcogenides. *Nature Phys.* (2015); online at doi:10.1038/nphys3434.
 101. Rahn, M. C., Ewings, R. A., Sedlmaier, S. J., Clarke, S. J. & A. T. Boothroyd, Strong $(\pi, 0)$ spin fluctuations in $\beta\text{-FeSe}$ observed by neutron spectroscopy. *Phys. Rev. B* **91**, 180501(R) (2015).
 102. Wang, Q. *et al.* Strong interplay between stripe spin fluctuations, nematicity and superconductivity in FeSe”, arXiv:1502.07544.
 103. Abrahams, E. & Si, Q. Quantum criticality in the iron pnictides and chalcogenides. *J. Phys.: Condens. Matter* **23**, 223201 (2011).
 104. Kasahara, S. *et al.* Evolution from non-Fermi- to Fermi-liquid transport via isovalent doping in $\text{BaFe}_2(\text{As}_{1-x}\text{P}_x)_2$ superconductors. *Phys. Rev. B* **81**, 184519 (2010).
 105. Löhneysen, H., Rosch, A., Vojta, M., & Wölfle, P. Fermi-liquid instabilities at magnetic quantum phase transitions. *Revs. Modern Phys.* **79**, 1015 (2007).
 106. Kadowaki, K. & Woods, S. Universal relationship of the resistivity and specific heat in heavy-fermion compounds. *Solid State Commun.* **58**, 507-509 (1986).
 107. Walmsley, P. *et al.* Quasiparticle Mass Enhancement Close to the Quantum Critical Point in $\text{BaFe}_2(\text{As}_{1-x}\text{P}_x)_2$. *Phy. Rev. Lett.* **110**, 257002 (2013).
 108. Ding, H. *et al.* Observation of Fermi-surface-dependent nodeless superconducting gaps in $\text{Ba}_{0.6}\text{K}_{0.4}\text{Fe}_2\text{As}_2$. *Europhys. Lett.* **83**, 47001 (2008).
 109. Xu, M. *et al.* Evidence for an *s*-wave superconducting gap in $\text{K}_x\text{Fe}_{2-y}\text{Se}_2$ from angle-resolved photoemission. *Phys. Rev. B* **85**, 220504 (2012).
 110. Ding, W., Yu, R., Si, Q. & Abrahams, E. Effective Exchange Interactions for Bad Metals and Implications for Iron-based Superconductors. arXiv:1410.8118.
 111. Goswami, P., Nikolic, P. & Si, Q. Superconductivity in Multi-orbital $t\text{-}J_1\text{-}J_2$ Model and its

- Implications for Iron Pnictides. *EuroPhys. Lett.* **91**, 37006 (2010).
112. Graser, S., Maier, T. A., Hirschfeld, P. J. & Scalapino, D. J. Near-degeneracy of several pairing channels in multiorbital models for the Fe pnictides. *New J. Phys.* **11**, 025016 (2009).
113. Kuroki, K. *et al.*, Unconventional Pairing Originating from the Disconnected Fermi Surfaces of Superconducting $\text{LaFeAsO}_{1-x}\text{F}_x$. *Phys. Rev. Lett.* **101**, 087004 (2008).
114. Wang, F., Zhai, H., Ran, Y., Vishwanath, A. & Lee, D.-H. Functional Renormalization-Group Study of the Pairing Symmetry and Pairing Mechanism of the FeAs-Based High-Temperature Superconductor. *Phys. Rev. Lett.* **102**, 047005 (2009).
115. Yu, R., Zhu, J.-X., and Si, Q. Orbital-selective superconductivity, gap anisotropy, and spin resonance excitations in a multiorbital t-J1-J2 model for iron pnictides. *Phys. Rev. B* **89**, 024509 (2014).
116. Ge, Q. *et al.*, Anisotropic but Nodeless Superconducting Gap in the Presence of Spin-Density Wave in Iron-Pnictide Superconductor $\text{NaFe}_{1-x}\text{Co}_x\text{As}$. *Phys. Rev. X* **3**, 011020 (2013).
117. Zhang, C. *et al.* Double spin resonances and gap anisotropy in superconducting underdoped $\text{NaFe}_{0.985}\text{Co}_{0.015}\text{As}$. *Phys. Rev. Lett.* **111**, 207002 (2013).
118. Zhang, C. *et al.* Neutron spin resonance as a probe of superconducting gap anisotropy in partially detwinned electron underdoped $\text{NaFe}_{0.985}\text{Co}_{0.015}\text{As}$. *Phys. Rev. B* **91**, 104520 (2015).
119. Nica, E., Yu, R. & Si, Q. Orbital selectivity and emergent superconducting state from quasi-degenerate *s*- and *d*-wave pairing channels in iron-based superconductors. arXiv:1505.04170.
120. Mou, D. *et al.* Distinct Fermi Surface Topology and Nodeless Superconducting Gap in a $(\text{Tl}_{0.58}\text{Rb}_{0.42})\text{Fe}_{1.72}\text{Se}_2$ Superconductor. *Phys. Rev. Lett.* **106**, 107001 (2011).
121. Wang, X. P. *et al.* Strong nodeless pairing on separate electron Fermi surface sheets in $(\text{Tl,K})\text{Fe}_{1.78}\text{Se}_2$ probed by ARPES. *Europhys. Lett.* **93**, 57001 (2011).
122. Wang, X.-P. *et al.* Observation of an isotropic superconducting gap at the Brillouin zone center of $\text{Tl}_{0.63}\text{K}_{0.37}\text{Fe}_{1.78}\text{Se}_2$. *Europhys. Lett.* **99**, 67001 (2012).
123. Park, J. T. *et al.* Magnetic Resonant Mode in the Low-Energy Spin-Excitation Spectrum of Superconducting $\text{Rb}_2\text{Fe}_4\text{Se}_5$ Single Crystals. *Phys. Rev. Lett.* **107**, 177005 (2011).
124. Friemel, G. *et al.* Reciprocal-space structure and dispersion of the magnetic resonant mode in the superconducting phase of $\text{Rb}_x\text{Fe}_{2-y}\text{Se}_2$ single crystals. *Phys. Rev. B* **85**, 140511(R) (2012).
125. Miao, H. *et al.* Observation of strong electron pairing on bands without Fermi surfaces in

- LiFe_{1-x}Co_xAs. *Nat. Commun.* **6**, 6056 (2015).
126. Niu, X. H. *et al.* Identification of prototypical Brinkman-Rice Mott physics in a class of iron chalcogenides superconductors. arXiv:1506.04018.
127. M. Gooch, B. Lv, B. Lorenz, A. M. Guloy & C.-W. Chu, Evidence of quantum criticality in the phase diagram of K_xSr_{1-x}Fe₂As₂ from measurements of transport and thermoelectricity. *Phys. Rev. B* **79**, 104504 (2009).
128. Ning, F. L. *et al.* Contrasting Spin Dynamics between Underdoped and Overdoped Ba(Fe_{1-x}Co_x)₂As₂. *Phys. Rev. Lett.* **104**, 037001 (2010).
129. Yoshizawa, M. *et al.* Structural Quantum Criticality and Superconductivity in Iron-Based Superconductor Ba(Fe_{1-x}Co_x)₂As₂. *J. Phys. Soc. Jpn.* **81**, 024604 (2012).
130. Ni, N. *et al.* Effects of Co substitution on thermodynamic and transport properties and anisotropic H_{c2} in Ba(Fe_{1-x}Co_x)₂As₂ single crystals. *Phys. Rev. B* **78**, 214515 (2008).
131. Chu, J.-H., Analytis, J. G., Kucharczyk, C., and Fisher, I. R. Determination of the phase diagram of the electron-doped superconductor Ba(Fe_{1-x}Co_x)₂As₂. *Phys. Rev. B* **79**, 014506 (2009).
132. Lester, C. *et al.* Neutron scattering study of the interplay between structure and magnetism in Ba(Fe_{1-x}Co_x)₂As₂. *Phys. Rev. B* **79**, 144523 (2009).
133. Nandi, S. *et al.* Anomalous Suppression of the Orthorhombic Lattice Distortion in Superconducting Ba(Fe_{1-x}Co_x)₂As₂ Single Crystals. *Phys. Rev. Lett.* **104**, 057006 (2010).
134. Zhou, R. *et al.* Quantum Criticality in Electron-doped BaFe_{2-x}Ni_xAs₂. *Nat. Commun.* **4**, 2265 (2013).
135. Lu, X. *et al.* Short-range cluster spin glass near optimal superconductivity in BaFe_{2-x}Ni_xAs₂. *Phys. Rev. B* **90**, 024509 (2014).
136. Yi, M. *et al.* Electron Correlation-Tuned Superconductivity in Rb_{0.8}Fe₂(Se_{1-z}S_z)₂. arXiv:1505.06636.
137. Reid, J.-Ph. *et al.* Universal Heat Conduction in the Iron Arsenide Superconductor KFe₂As₂: Evidence of a d -Wave State. *Phys. Rev. Lett.* **109**, 087001 (2012).
138. Okazaki, K. *et al.* Octet-Line Node Structure of Superconducting Order Parameter in KFe₂As₂. *Science* **337**, 1314 (2012).
139. Hong, X. C. *et al.* Nodal gap in iron-based superconductor CsFe₂As₂ probed by quasiparticle heat transport. *Phys. Rev. B* **87**, 144502 (2013).

140. Zhang, Z. *et al.* Heat transport in RbFe₂As₂ single crystals: Evidence for nodal superconducting gap. *Phys. Rev. B* **91**, 024502 (2015).
141. Hardy, F. *et al.* Evidence of Strong Correlations and Coherence-Incoherence Crossover in the Iron Pnictide Superconductor KFe₂As₂. *Phys. Rev. Lett.* **111**, 027002 (2013).
142. Wang, A. F. *et al.* Calorimetric study of single-crystal CsFe₂As₂. *Phys. Rev. B* **87**, 214509 (2013).
143. Eilers, F. *et al.* Quantum criticality in AFe₂As₂ with A = K, Rb, and Cs suppresses superconductivity. arXiv:1510.01857.
144. Yi, M. *et al.* Electronic reconstruction through the structural and magnetic transitions in detwinned NaFeAs. *New J. Phys.* **14**, 073019 (2012).
145. Böhmer, A. E. *et al.* Nematic Susceptibility of Hole-Doped and Electron-Doped BaFe₂As₂ Iron-Based Superconductors from Shear Modulus Measurements. *Phys. Rev. Lett.* **112**, 047001 (2015).
146. Thorsmolle, V. K. *et al.* Critical Charge Fluctuations in Iron Pnictide Superconductors. arXiv:1410.06116.
147. Kretzschmar, F. *et al.* Nematic fluctuations and the magneto-structural phase transition in Ba(Fe_{1-x}Co_x)₂As₂. arXiv:1507.06116.
148. Song, Y. *et al.* Energy dependence of the spin excitation anisotropy in uniaxial-strained BaFe_{1.9}Ni_{0.1}As₂. *Phys. Rev. B* **92**, 180504 (R) (2015).
149. Anisimov, V. I. *et al.* Orbital-selective Mott-insulator transition in Ca_{2-x}Sr_xRuO₄. *Eur. Phys. J. B* **25**, 191-201 (2002).
150. Neupane, M. *et al.* Observation of a Novel Orbital Selective Mott Transition in Ca_{1.8}Sr_{0.2}RuO₄. *Phys. Rev. Lett.* **103**, 097001 (2009).
151. Hosono, H. & Kuroki, K. Iron-based superconductors: Current status of materials and pairing Mechanism. *Physica C* **514**, 399 (2015).